PHYSICAL REVIEW B VOLUME 47, NUMBER 15 15 APRIL 1993-I

Electronic charge distribution in crystalline diamond, silicon, and germanium

Z. W. Lu and Alex Zunger
National Renewable Energy Laboratory, Golden, Colorado 80401

Moshe Deutsch
Department of Physics, Bar Ilan University, Ramat-Gan 52900, Israel
(Received 3 November 1992)

Recent refinement studies of a consolidated set of Si structure factors have produced information on the Si charge density with an unprecedented level of accuracy, unmatched by any other crystallographic study to date. In this work we examine the extent to which an accurate implementation of the local-density formalism can describe the charge distribution in silicon, as well as that of the experimentally less-refined data on diamond and germanium. Results of a refinement study of recent germanium and diamond measurements are presented and compared with the *ab initio* calculations. Our *ab initio* calculated structure factors for Si show a twofold to fivefold improvement in the R factor over previous local-density calculations. We describe in detail, total, valence, and deformation charge-density maps for C, Si, and Ge. We analyze the effects of high-momentum components (currently outside the range of the high-precision measurements) as well as dynamic structure factors on the ensuing charge-density maps.

I. INTRODUCTION

Recent advances in measurements and analyses have now produced extremely accurate data on the charge distribution in crystalline silicon:[1–7] Cummings and Hart[1] have recently consolidated five data sets of high-precision Si structure factors obtained in three independent experiments by Aldred and Hart,[2] Teworte and Bonse,[3] and Saka and Kato.[4] The data were corrected for anomalous dispersion (using *measured*, wavelength-dependent dispersion factors) and nuclear scattering, and careful consistency checks and error estimates were conducted. More recently, Deutsch[5,6] fitted this consolidated and corrected data set of silicon structure factors to a parametrized model in which the harmonic and anharmonic thermal effects were deconvoluted from the static charge density. As a result of these recent developments, (i) the structure factors of Si are now known to a *milli-electron level of accuracy*, better by one order of magnitude or more than any other crystal studied to date[6] and (ii) the static charge-density map of Si (Refs. 5 and 6) is now known with an unprecedented level of detail. In view of these developments we have decided to (i) examine the extent to which the local-density formalism,[8,9] implemented with the highest computational precision possible to date, is able to capture the details of the highly accurate measured Si structure factors and charge density, and (ii) perform a similar data refinement as done for Si by Deutsch for the (far less complete and accurate) data sets on diamond and germanium, so that chemical trends along the C→Si→Ge sequence can be assessed.

There are many previous calculations of the Si charge density. These include the empirical pseudopotential calculations by Walter and Cohen,[10] Chelikowsky and Cohen,[11] Bertoni *et al.*,[12] and Balderschi *et al.*;[13] the local semiempirical pseudopotential calculation of Hamann;[14] and the first-principles nonlocal pseudopotential calculations by Zunger and Cohen,[15] Zunger,[16] Ihm and Cohen,[17] Yin and Cohen,[18] and Nielsen and Martin.[19] All-electron calculations of the Si charge density include the orthogonalized-plane-waves (OPW) calculation by Stukel and Euwema[20] and by Raccah *et al.*,[21] the linear combination of Gauss orbital (LCGO) by Wang and Klein,[22] and Heaton and Lafon,[23] and the linear muffin-tin orbital (LMTO) calculations by Weyrich,[24] Methfessel, Rodriguez, and Andersen,[25] and Polatoglou and Methfessel.[26] In addition to the calculations that use the local-density approximation,[14–26] there exists the Hartree-Fock calculation by Dovesi, Causa, and Angonoa[27] and by Pisani, Dovesi, and Orlando.[28] Furthermore, Balbás *et al.*[29] have calculated the structure factors of Si using model bond-charge density examining the role of different approximations to the exchange-correlation potential. The reasons that we undertook a recalculation of the Si charge density despite these many previous works are fourfold.

First, all of the previous calculations were published before the completion of the analysis of the high-precision Si data by Cummings and Hart[1] and by Deutsch,[5,6] so none includes a comparison with these data. Furthermore, none of the previous authors have published both structure factors, as well as valence and deformation charge-density maps.

Second, many of the previous calculations have incorporated computational approximations whose effects on the charge density remain, in many cases, untested. These include the pseudopotential approximation,[10–18] use of limited basis sets,[22,23,27] or perturbation theory.[12] Spackman[30] has recently compared the predictions of many of these calculations with a few measured (pre-

Cummings and Hart) structure factors, finding significant discrepancies for all except the OPW results of Stukel and Euwema.[20] We wish to perform an analogous comparison with the current data, using calculated results in which the convergence parameters of the theory are controllably pushed to the limit where the results reflect as much as possible the predictions of the underlying (local-density) Hamiltonian, unobscured by computational uncertainties.

Third, we wish to examine a number of assumptions that have traditionally been made in the transformation of structure factors to charge-density plots. These include (i) the assumption that high-momentum Fourier components (which are difficult to measure with high precision) reflect merely *core* contributions and are therefore inconsequential for describing the *valence* charge density or the solid versus atom density differences. There are, however, indications[31,32] that the nodal structure in the latter quantities may also require high-momentum components, currently outside the reach of high-precision measurements. Also (ii), it is often assumed (e.g., Zuo, Spence, and O'Keefe[33]) that even if the high-Fourier components in the *static* charge-density difference are non-negligible, the Debye-Waller factor will attenuate them, so that the *dynamic* density difference map will not require high-momentum components. We wish to examine this hypothesis by comparing static and dynamic charge-density difference maps for a range of increasing momentum cutoff values.

Finally, while the measured x-ray structure factors of diamond[34–39] and germanium[40–43] are significantly less accurate[44,45] than those available now for Si, global trends in the measurement and model-refined structure factors can nevertheless be established. We note that previous analysis of the Si data[5,6] revealed a vanishing anharmonic temperature term ($\beta = 0$) and a different Debye-Waller factor for core and valence electrons. It would be interesting to examine these points also for diamond and germanium. We will hence subject the experimental data to the same analysis done for Si and to examine the trends in the ensuing charge densities in the C→Si→Ge series. Comparison with previous calculations on C and Ge will then be discussed.

The plan for the balance of this paper is as follows. Section II defines the measured quantities to be discussed below and analyzes these quantities for C and Ge thus producing a separation of static versus dynamic densities. Section III describes the calculated counterparts. Section IV defines the core, valence, and total charge densities and their respective deformation charge densities. Section V examines the convergence of the current calculations. Section VI presents the comparison of theory with experiment. Finally, Sec. VII provides a summary of the findings of the present study.

II. MEASURED QUANTITIES AND THEIR MODELING

In this section we define all of the quantities shown later in our tables and figures. We will consistently denote dynamic and static charge densities as F and ρ, respectively, and label Fourier transforms for a momentum $\mathbf{G} = \frac{2\pi}{a}(h,k,l)$ as $F(\mathbf{G})$ or $\rho(\mathbf{G})$, while real-space densities will be denoted as $F(\mathbf{r})$ and $\rho(\mathbf{r})$.

A. Dynamic structure factors and densities

Dawson[46] has shown that if the "rigid-atom approximation" is invoked, the dynamic structure factors $F_{\text{expt}}(\mathbf{G})$ can be represented as a convolution of the αth site static structure factor $\rho_\alpha(\mathbf{G})$ and the dynamic temperature "smearing function" $T_\alpha(\mathbf{G})$ as

$$F_{\text{expt}}(\mathbf{G}) = \sum_{\alpha=1}^{M} \rho_\alpha(\mathbf{G}) e^{i\mathbf{G}\cdot\boldsymbol{\tau}_\alpha} T_\alpha(\mathbf{G}) \ , \tag{1}$$

where $\rho_\alpha(\mathbf{G})$ is the $\mathbf{G}$th Fourier component of the static charge density contributed by atomic site α (whose position vector in the unit cell is $\boldsymbol{\tau}_\alpha$), and $T_\alpha(\mathbf{G})$ is the α's site dynamic (temperature) smearing function containing harmonic and anharmonic terms. $T_\alpha(\mathbf{G})$ is often approximated by the Debye-Waller factor $\exp(-G^2 B_\alpha/16\pi^2)$. Note that the approximation of Eq. (1) implies a linear partitioning of the continuous three-dimensional charge density into subregions associated with identifiable scattering centers α. This partitioning is referred to as the rigid-atom approximation. Within this approximation, it is possible to fit the data either with a single Debye-Waller factor or by assigning different B's to different atomic shells ("the independent shell vibrational model").

The *dynamic* real-space charge density can be synthesized from the Fourier components of Eq. (1) by summing them (after subtracting anomalous scattering corrections) to a maximum momentum $\mathbf{G}_{\max}$ accessible from diffraction experiments. This gives

$$F_{\text{expt}}(\mathbf{r}, \mathbf{G}_{\max}) = \sum_{\mathbf{G}}^{\mathbf{G}_{\max}} F_{\text{expt}}(\mathbf{G}) e^{i\mathbf{G}\cdot\mathbf{r}} \ , \tag{2}$$

where the result naturally depends on the highest momentum ($\mathbf{G}_{\max}$) included in this sum. Fourier truncation effects underlying Eq. (2) could affect the shape of the ensuing charge-density map.

B. Static structure factors and Dawson's model

For purposes of comparison with the results of quantum-mechanical calculations it is often desirable to deconvolute Eq. (1) thus finding the *static* (purely electronic) structure factor

$$\rho_{\text{expt}}(\mathbf{G}) = \sum_{\alpha=1}^{M} \rho_\alpha(\mathbf{G}) e^{i\mathbf{G}\cdot\boldsymbol{\tau}_\alpha} \ . \tag{3}$$

For monatomic crystals in the harmonic rigid-atom approximation, this deconvolution could be done by multiplying $F_{\text{expt}}(\mathbf{G})$ by the inverse Debye-Waller factor

$$\rho_{\text{expt}}(\mathbf{G}) = F_{\text{expt}}(\mathbf{G}) e^{BG^2/16\pi^2} \ . \tag{4a}$$

The resulting $\rho_{\text{expt}}(\mathbf{G})$ are then summed giving the static

Fourier-synthesized total density map

$$\rho_{\rm expt}(\mathbf{r},\mathbf{G}_{\rm max})=\sum_{\mathbf{G}}^{\mathbf{G}_{\rm max}}\rho_{\rm expt}(\mathbf{G})e^{i\mathbf{G}\cdot\mathbf{r}}\ . \tag{4b}$$

The precision of this map is naturally limited by the largest momentum component accessible to high-precision measurements as well as the validity of the aforementioned rigid-atom approximation. An alternative method whose precision depends to a lesser extent on the explicit convergence of Eq. (4b) (still using the rigid-atom approximation) was outlined by Dawson[46] and refined by Stewart,[47,48] Coppens *et al.*,[49] and Deutsch.[5,6] The approach is based on the fact that any ground-state crystalline properties such as $\rho_\alpha(\mathbf{r})$ of Eq. (1) can be rigorously expanded in an infinite set of orthonormal Kubic harmonics $K_l^{a_1}(\hat{r})$ of angular momentum l belonging to the totally symmetric (a_1) representation of the αth site group

$$\rho^{(\alpha)}_{\rm model}(\mathbf{r})=\sum_{l=0}^{\infty}R_l(r)K_l^{a_1}(\hat{r})\ . \tag{5}$$

Here r and $\hat{r}$ are the modulus and direction, respectively, of $\mathbf{r}$ and $R_l(r)$ are the αth site radial functions defined by the convolution of the exact $\rho_\alpha(\mathbf{r})$ with $K_l^{a_1}(\hat{r})$. For the T_d site symmetry of the diamond lattice, the symmetry-allowed l values are $l=0$, 3, 4, 6, 7, 8,... . The $l=0$ term is the spherical contribution whereas $l=$ odd and $l=$ even are antisymmetric and centrosymmetric contributions, respectively. Conventional x-ray refinement techniques[50] retain but the spherical term in Eq. (5) (using the superposition of spherical atom densities). Dawson's method consists of truncating Eq. (5) to include only the leading terms $l=0$, 3, and 4 and suggesting convenient analytic guesses for the atom-localized radial functions $R_l(r)$. Deutsch[5,6] and Spackman[44] used

$$R_{l=0}(r)=4\pi\sum_{nl}\kappa_{nl}^3 n_{nl}(\kappa_{nl}r)\ , \tag{6a}$$

and

$$R_{l=3,4}(r)=A_l r^{\lambda_l}e^{-\xi r}\ , \tag{6b}$$

where κ_{nl}, A_l, λ_l, and ξ are adjustable parameters and n_{nl} are the fixed ground-state atomic (usually Hartree-Fock) charge densities[51,52] for orbitals nl. The parameters κ_{nl} are intended to model monopole expansion or contraction of the spherical atomic charge densities due to bonding. One further parametrizes $T_\alpha(\mathbf{G})$ in terms of the Debye-Waller factor B_{nl} for orbital nl and a small anharmonic potential of magnitude β. Inserting into Eq. (1) the Fourier transform $\rho_{\rm model}(\mathbf{G})$ of the model density of Eqs. (5) and (6) and the model dynamic temperature factors $T_\alpha(\mathbf{G})$ then gives an analytic Fourier-space representation of $F_{\rm model}(\mathbf{G})$ in terms of the parameter set $\{\kappa_{nl},\lambda_l,A_l,\xi,B_{nl},\beta\}$. These parameters are then determined by a least-squares fit of the $\{F_{\rm model}(\mathbf{G})\}$ to the set $\{F_{\rm expt}(\mathbf{G})\}$. Using Eqs. (5) and (6) this gives the αth site real-space model density $\rho^{(\alpha)}_{\rm model}(\mathbf{r})$ and its Fourier transform $\rho^{(\alpha)}_{\rm model}(\mathbf{G})$. One can then proceed and obtain the *total* crystalline model density in two ways. In the first approach used originally by Dawson[46] and subsequently by other practitioners of this model,[5,6,47–49] one superposes the *real-space* atomic model density $\rho^{(\alpha)}_{\rm model}(\mathbf{r})$ over all lattice sites $\mathbf{R}_j$,

$$\rho_{\rm model}(\mathbf{r})=\sum_{j}^{\infty}\sum_{l=0,3,4}R_l(\mathbf{r}-\mathbf{R}_j)K_l(\hat{r}-\hat{\mathbf{R}}_j)\ . \tag{7a}$$

This density contains a contribution corresponding to arbitrary large momentum components despite the fact that only a limited set of structure factors $\{F_{\rm expt}(\mathbf{G});\mathbf{G}\le\mathbf{G}_{\rm max}\}$ are used to fit the model parameters. This approach is hence *extrapolative*: the nonzero values of $\rho_{\rm model}(\mathbf{G}>\mathbf{G}_{\rm max})$ are implicitly determined by the choice of the form and number of model functions $R_l(r)$. The second alternative is to construct a truncated Fourier series from the model density, analogous to Eq. (4b)

$$\rho_{\rm model}(\mathbf{r},\mathbf{G}_{\rm max})=\sum_{\mathbf{G}}^{\mathbf{G}_{\rm max}}\left\{\sum_{\alpha=1}^{M}\rho^{(\alpha)}_{\rm model}(\mathbf{G})e^{i\mathbf{G}\cdot\tau_\alpha}\right\}e^{i\mathbf{G}\cdot\mathbf{r}}\ . \tag{7b}$$

In this approach all unmeasured structure factors ($\mathbf{G}>\mathbf{G}_{\rm max}$) are taken to be zero.

Finally, in addition to the adjustable parameters in Dawson's model, one has to choose the "fixed" quantities, e.g., the orbital densities $n_{nl}(r)$. These could be atomic Hartree-Fock orbitals or local-density orbitals, relativistic or nonrelativistic orbitals, as well as "canonical" versus rotated orbitals. We will examine below the implications and consequences of these choices.

C. Fitting Dawson's model to experiment

The consolidated data set of Cummings and Hart[1] for Si was fit to Dawson's model by Deutsch.[5,6] His best fit ("model p" in Ref. 6) produces a remarkably low R factor of 0.036% and a goodness of fit (GoF) of 1.20. This represents the most accurately determined crystalline structure to date. Table I gives the model parameters obtained in this fit (the error in the exponent ξ of Ref. 6 is corrected in Table I and the remainder of this paper. The correct value is $\xi=2.285$ a.u.$^{-1}$). The results show an expansion of $\sim 6\%$ of the $3sp$ valence shell and of $\sim 0.5\%$ of the core $2sp$ shell. The best fit is obtained when the crystal-bound silicon atom is permitted to have a shell-dependent Debye-Waller parameters $B_{\rm val}\le 0.11$ Å^2 and $B_{\rm core}$=0.4585 Å^2. No evidence is found for an anharmonic term in the effective potential of the atom, i.e., $\beta=0$. Further details are given in Refs. 5 and 6. We next describe our analogous fits for diamond and germanium.

1. *Fits for diamond*

Two data sets are available here: the nine single-crystal structure factors of Takama, Tsuchiya, Kobayashi, and Sato [(TTKS), Ref. 39] measured by the Pendellösung

TABLE I. Parameters obtained by fitting Dawson's model [Eqs. (5) and (6)] to the observed structure factors of C, Si, and Ge. For C and Si we use Clementi's (Ref. 51) nonrelativistic orbital densities n_{nl}, while for Ge we use both Clementi's nonrelativistic (NR) orbital densities as well as the relativistic LDA results. In all cases we use $\lambda_l = 4$ for all l values. An asterisk indicates that quantity was held fixed during the fit. The value $\xi = 2.435$ for Si in Ref. 6 was in error; the correct value is given here. We also give R value and goodness of fit (GoF) for the fit.

	κ Core	κ Valence	ξ (a.u.$^{-1}$)	A_3 (e)	A_4 (e)	B_{core} (Å^2)	B_{val} (Å^2)	β (eV/Å^3)	R (%)	GoF
Diamond										
TTKS data[a]	1*	1*	3.541	0.334	0*	0.1379	0.1379	0*	0.706	4.25
GW data[b]	1*	0.99	3.259	0.343	−0.275	0.2303	0.2303	0*	0.793	3.03
Silicon[c]	0.9949	0.9382	2.285	0.4484	−0.1270	0.4585	0.0	0*	0.036	1.20
Germanium										
NR,Clementi[d]	1*	1*	1.877	0.591	−0.571	0.5474	0.5474	1.8*	0.188	1.03
Relativistic[e]	1*	0.9553	1.913	0.583	−0.510	0.5654	0.5654	0.9*	0.189	1.07

[a] 9 **G** values from Ref. 39, plus F_{222} taken from Ref. 37.

[b] 24 **G** values from Ref. 36. We use Eq. (8) where the scale factor is $S = 1.021$ and $F_{\text{bg}} = 0.039$.

[c] 18 **G** values from the CH data of Ref. 6; note that for the core states, $\kappa_{n=1} = 1.0$ and $\kappa_{n=2} = 0.9949$.

[d] 12 **G** values from MK (Ref. 40) and DHC (Ref. 43). We use Eq. (8) where the scale factors are $S_1 = 1.015$ for MK and $S_2 = 1.003$ for DHC and $F_{\text{bg}} = 0$.

[e] 12 **G** values from MK (Ref. 40) and DHC (Ref. 43). We use Eq. (8) where the scale factors are $S_1 = 1.010$ for MK and $S_2 = 0.999$ for DHC, and $F_{\text{bg}} = 0$.

method, and the older (1959) powder data of Göttlicher and Wölfel [(GW), Ref. 36] obtained for 24 reflections. Dispersion corrections and nuclear scattering are negligible for both data sets. Both data sets have problems: possible crystal imperfections observable in topography of the crystal used (TTKS), and a powder technique requiring many corrections (GW). The structure factors measured by TTKS are consistently larger than those of GW except for the (111) reflection. The measured $F(311)$ structure factor of TTKS of $1.648e$/atom compares well with a previous single-crystal measurement of Lang and Mai[38] giving $1.630e$/atom, while GW found a considerably lower $F(311) = 1.592e$/atom.

Spackman[44] fitted the TTKS data [adding to these the (222) reflection from Ref. 37] to Dawson's model, finding $R = 0.85\%$ and the goodness of fit equal to 4.26. We have refitted these data for two reasons. First, Spackman used the *rotated* atomic-orbital densities $n_{nl}(r)$ [Eq. (6a)] of Stewart[52] rather than the canonical Clementi results.[51] While these sets are related by a unitary transformation (hence, they produce the same *total* density), the valence-only results differ significantly: Stewart's orbitals produce a local *minimum* on the atomic sites, while Clementi's orbitals produce a *maximum* on the atomic sites (see below) outside the atomic regions; the two representations are similar. Since the Si data were fitted with Clementi orbitals, for reasons of consistency we will use these also for diamond and germanium. Second, Spackman used in Eq. (6b) the exponents $\lambda_3 = 3$ and $\lambda_4 = 4$ for diamond and $\lambda_3 = 6$ for germanium. Since $\lambda_3 = \lambda_4 = 4$ gave the best results for Si,[6] we will use these fixed values also for diamond and germanium. While other choices for λ_l were also tried, these seem to yield the best overall fits.

Our best-fit results for the ten points TTKS set for diamond are given in Table I. The quality of the fit (R factor) is similar to that obtained by Spackman. Table I also gives the results of the fit to the 24 points GW data set. In this case, it is necessary to introduce a fixed scaling factor (S) and a constant background contribution (F_{bg}) to the measured data $F_{\text{obs}}(\mathbf{G})$, i.e.,

$$F_{\text{expt}}(\mathbf{G}) = SF_{\text{obs}}(\mathbf{G}) - F_{\text{bg}} \ . \tag{8}$$

Table I shows that while both data sets give the best fit for a zero anharmonic factor $\beta = 0$ and a single Debye-Waller factor, they differ in detail: the fit to the TTKS set produces a 50% smaller Debye-Waller factor and gives no indication of the $l = 4$ contribution to the density. In contrast, the fit to the GW data set gives a significant $l = 4$ component and a small expansion of the valence shell. We will compare below both results to *ab initio* calculations.

2. *Fits for germanium*

Three recent data sets are available here: Takama and Sato [(TS), Ref. 42], Matsushita and Kohra [(MK), Ref. 40], and Deutsch, Hart, and Cummings [(DHC), Ref. 43]. All other available structure factors were measured on powders and have lower accuracies. Here, unfortunately, there is no consolidated set of structure factors. Furthermore, all data sets were measured at different wavelengths, so dispersion corrections f' need to be applied before comparison or averaging can be done. There are no measured f' values for any of the three sets. The Cromer-Liberman calculated values[53,54] are highly uncertain, e.g., in Si, they were off by 30–40% from directly measured f' values using Mo and Ag radiations.[55] For Ge with Cu radiation (MK measurements), which is very close to the edge, the f' value is large, and any error in it represents a large error in the striped F value. We

find that when the f' values are subtracted, using the best estimate of the Debye-Waller factor, there are fairly large deviations between the three sets for the common (hkl)'s.

One approach to the problem taken by Brown and Spackman[45] is to combine the sets in a somewhat arbitrary fashion. They use the MK set but replace the (111) and add the (511) values by those of TS, scaled by the average ratios of the common reflections in the two sets. The analysis of Brown and Spackman did not consider the DHC set, which was not yet published at that time.

We have adopted a different approach. We fit the structure factors of TS and MK separately with the same "standard" model $\{B, \xi, A_3, A_4, S\}$, where S is a scale factor [Eq. (8)], common to all F's of a set as in Ref. 45. The residuals for MK were 1.5–2 times smaller than for TS. Consequently, we adopted the set of MK as it is with no replacement or additions from scaled values of TS. However, we added to this set the DHC set, which has a few (hkl) in common with MK and a few higher-order reflections, which are important for the determination of B. Where common (hkl) exist, both were included in the set. The fit of the standard model to this combined set (using of course two S's; one for MK and one for DHC) did not show any systematic trends in the residuals, which remained all of the same average magnitude as for the MK set alone.

The number of F's in the measured set is 14, with some hkl having two measured values. The f' values used are those of Creagh[55] for the MK data ($f' = -1.089$), and those of DHC (Ref. 43) for their data ($f' = 0.09$). These were fixed in all fits.

Since Ge is a rather heavy element ($Z = 32$), one might expect relativistic effects to be non-negligible in the calculated charge densities and structure factors. This is indeed born out by the comparison of the local-density-approximation (LDA) nonrelativistic (NR) atomic structure factors with their relativistic (R) counterparts shown in Table II. Both sets of structure factors were calculated from numerical integration of the local-density equations using the spin-polarized Ceperley-Alder exchange-correlation[56] and the s^2p^2 configuration. The corresponding relativistic corrections for carbon and silicon are negligible. Table II shows also the Hartree-Fock (HF) atomic results.[57,51] We see that whereas the relativistic correction $n_R(q) - n_{\rm NR}(q)$ is similar in the LDA and HF results, there are differences between the absolute values of $n(q)$ as calculated by HF and the LDA. These reflect the absence of correlation in the HF calculation and the different nature of the exchange potential (local versus nonlocal in the LDA and HF results, respectively). Since there are no tabulations of orbital-by-orbital Hartree-Fock relativistic densities $n_{nl}(r)$ for Ge, the relativistic fits were done using LDA orbitals.

Table I gives the results of the fit to the Ge data using relativistic LDA orbitals. The table also gives the results obtained with the conventional (nonrelativistic) Clementi Hartree-Fock orbitals. We see that the statistical quality of both fits are nearly the same. However, as shown below, the relativistic fit produces much better agreement with (i) the measured forbidden (442) and (622) reflections and (ii) the *calculated* crystal structure factors. Thus, we will use below mostly the results of

TABLE II. Calculated free-atom germanium structure factors $n(q)$ for momentum $q = \sin\theta/\lambda$ as obtained in the local-density approximation (LDA) and the Hartree-Fock (HF) approximation. We list the nonrelativistic (NR) values, as well as the relativistic (R) correction $n_R(q) - n_{\rm NR}(q)$.

q (Å^{-1})	LDA $n_{\rm NR}(q)$	HF[a] $n_{\rm NR}(q)$	LDA $n_R(q) - n_{\rm NR}(q)$	HF[b] $n_R(q) - n_{\rm NR}(q)$
0.05	31.278	31.278	0.006	−0.002
0.10	29.540	29.527	0.019	0.007
0.15	27.498	27.477	0.029	0.027
0.20	25.532	25.532	0.031	0.035
0.25	23.722	23.759	0.028	0.032
0.30	22.040	22.109	0.024	0.027
0.35	20.450	20.536	0.023	0.024
0.40	18.934	19.021	0.026	0.026
0.50	16.130	16.188	0.040	0.039
0.60	13.699	13.716	0.054	0.054
0.70	11.695	11.681	0.064	0.064
0.80	10.114	10.083	0.068	0.068
0.90	8.906	8.870	0.067	0.067
1.00	7.997	7.963	0.065	0.065
1.10	7.313	7.286	0.062	0.062
1.20	6.789	6.770	0.059	0.060
1.30	6.371	6.361	0.059	0.058
1.40	6.020	6.018	0.060	0.058
1.50	5.710	5.714	0.061	0.060

[a]Reference 51.
[b]Reference 57.

relativistic fits, although we will comment on the comparison with the nonrelativistic fits.

We find that Ge exhibits a clear anharmonic term β; its value (0.9) is comparable to the measured values of Tischler and Batterman of (1.27±0.25) (Ref. 58) and Roberto, Batterman, and Keating of (1.50±0.22).[59] The nonrelativistic fit also indicates a nonzero β, which, although twice as large, is still in reasonable accord with experiment. The relativistic fit shows a 4.5% expansion of the valence shell compared with the 6% expansion found for silicon. No evidence was found in either fit for a shell-dependent Debye-Waller factor of the sort found for silicon. However, as these conclusions are based on a set of measured structure factors of germanium which is both smaller and less accurate than that of silicon, further higher accuracy measurements are needed to confirm the validity of this conclusion.

III. CALCULATED QUANTITIES

A. Static structure factors and densities

While diffraction experiments produce discrete Fourier components of the charge density, electronic structure calculations produce the total static electron charge density $\rho_{\rm calc}(\mathbf{r})$ directly in coordinate space. This is obtained by summing the squares of the one-electron crystalline wave function over all occupied band indices i and Brillouin-zone wave vectors $\mathbf{k}$ enclosed within the Fermi energy ε_F

$$\rho_{\rm calc}(\mathbf{r}) = \sum_{i,\mathbf{k}}^{\varepsilon_F} N_i(\mathbf{k})\psi_i^*(\mathbf{k},\mathbf{r})\psi_i(\mathbf{k},\mathbf{r}) \ , \tag{9}$$

where $N_i(\mathbf{k})$ is the occupation numbers of band i at momentum $\mathbf{k}$. The Fourier components of the static charge density can then be computed from

$$\rho_{\rm calc}(\mathbf{G}) = \frac{1}{\Omega}\int \rho_{\rm calc}(\mathbf{r})e^{-i\mathbf{G}\cdot\mathbf{r}}d\mathbf{r} \ , \tag{10}$$

where Ω is the unit-cell volume. To compare with the experimental static charge density $\rho_{\rm expt}(\mathbf{r},\mathbf{G}_{\rm max})$ of Eq. (4b) one can then filter out all Fourier components above a given momentum value of $\mathbf{G}_{\rm max}$, finding

$$\rho_{\rm calc}(\mathbf{r},\mathbf{G}_{\rm max}) = \sum_{\mathbf{G}}^{\mathbf{G}_{\rm max}} \rho_{\rm calc}(\mathbf{G})e^{i\mathbf{G}\cdot\mathbf{r}} \ . \tag{11}$$

Note that Eqs. (9) and (11) differ by Fourier truncation effects, which will be examined below.

B. Dynamic structure factors and densities

Comparison of calculated quantities with the measured $F_{\rm expt}(\mathbf{G})$ of Eq. (1) requires the introduction of the dynamic factor $T_\alpha(\mathbf{G})$ into the calculation. The obvious difficulty here is that while the *measured* structure factors analyzed through the rigid-atom approximation [Eq. (1)] represent linear contributions from discrete scattering centers α, there is no *unique* way of partitioning the *calculated* three-dimensional density $\rho_{\rm calc}(\mathbf{r})$ of Eq. (9) into atomic-centered quantities. One common practice[60,61] is to replace $T_\alpha(\mathbf{G})$ by some average $\langle T(\mathbf{G})\rangle$ over the different atomic species α in the unit cell, then [in analogy with Eq. (4a)] factor $\langle T\rangle$ out of Eq. (1). While this procedure seems reasonable when the bonded atoms have similar vibrational properties (hence, similar Debye-Waller factors), it is not obvious how accurate it is otherwise. Given that any partitioning of $\rho(\mathbf{r})$ into atomically centered quantities is arbitrary, we will choose a physically appealing but, much like Eq. (1), nonunique scheme: having calculated a unique and continuous density $\rho_{\rm calc}(\mathbf{r})$ from Eq. (9), we decompose it into (i) "muffin-tin" (MT) spheres around each atom α and (ii) the remaining, interstitial volume between them. Denoting as $\rho_\alpha^{\rm MT}(\mathbf{G})$ the Fourier transform of the MT charge density in the α's muffin-tin sphere (minus the extrapolation of the interstitial charge density into this sphere) and by $\rho_I(\mathbf{G})$ the Fourier transform of the interstitial (I) charge density over all space, the calculated dynamic structure factor becomes

$$F_{\rm calc}(\mathbf{G}) = \rho_I(\mathbf{G})e^{-\langle B\rangle G^2/16\pi^2} + \sum_{\alpha=1}^{M}\rho_\alpha^{\rm MT}(\mathbf{G})e^{-B_\alpha G^2/16\pi^2} \ , \tag{12a}$$

where B_α are the measured Debye-Waller factors and $\langle B\rangle$ is their atomic average. The terms of Eq. (12a) are calculated in a way that avoids taking Fourier transforms of abruptly truncated functions. Note that for a monatomic crystal such as C, Si, and Ge we have $\langle B\rangle = B$ and $M = 1$, so

$$F_{\rm calc}(\mathbf{G}) = \rho_{\rm calc}(\mathbf{G})e^{-BG^2/16\pi^2} \ , \tag{12b}$$

and the partitioning of Eq. (12a) is not needed. The corresponding calculated dynamic charge-density map is then

$$F_{\rm calc}(\mathbf{r},\mathbf{G}_{\rm max}) = \sum_{\mathbf{G}}^{\mathbf{G}_{\rm max}} F_{\rm calc}(\mathbf{G})e^{i\mathbf{G}\cdot\mathbf{r}} \ , \tag{13}$$

which can be compared with $F_{\rm expt}(\mathbf{r},\mathbf{G}_{\rm max})$ of Eq. (2).

IV. PARTITIONING THE CHARGE DENSITY

In order to assess bonding effects, it has been customary[50] to subtract from $\rho(\mathbf{r})$ a superposition (sup) of calculated ground-state spherical charge densities of the neutral free atoms. The Fourier components of this reference charge density are

$$\rho_{\rm sup}(\mathbf{G}) = \sum_{\alpha=1}^{M} n_\alpha(\mathbf{G})e^{i\mathbf{G}\cdot\boldsymbol{\tau}_\alpha} \ , \tag{14}$$

where $n_\alpha(\mathbf{G})$ is the Fourier transform of the αth free-atom charge density [not to be confused with the crystalline quantity $\rho_\alpha(\mathbf{G})$ of Eq. (1) which pertains to bonded atoms]. The dynamic superposition structure factors are then

$$F_{\rm sup}(\mathbf{G}) = \sum_{\alpha=1}^{M} n_\alpha(\mathbf{G})e^{i\mathbf{G}\cdot\boldsymbol{\tau}_\alpha}T_\alpha(\mathbf{G}) \ . \tag{15}$$

Note that if bonding effects modify the core density relative to that in the free atom, even the high Fourier components of $\rho_{\rm sup}(\mathbf{G})$ will differ from $\rho_{\rm calc}(\mathbf{G})$. In order to isolate such effects it is further customary to decompose ρ into "core" and "valence" terms. The sum over states $(i,\mathbf{k})$ in Eq. (9) can be partitioned into

$$\rho_{\rm calc}(\mathbf{r}) = \rho_{\rm core}(\mathbf{r}) + \rho_{\rm val}(\mathbf{r}) \ , \tag{16}$$

where

$$\rho_{\rm val}(\mathbf{r}) = \sum_{i\neq \rm core} \sum_{\mathbf{k}} N_i(\mathbf{k}) \psi_i^*(\mathbf{k},\mathbf{r}) \psi_i(\mathbf{k},\mathbf{r}) \ , \tag{17a}$$

and core is $1s$ for diamond, $1s$, $2s$, $2p$ for Si, and $1s$, $2s$, $2p$, $3s$, $3p$, $3d$ for Ge. This partitioning is based on the fact that there is a significant energy separation in the band structure between core and valence states. Using this partitioning, it is possible to assign different Debye-Waller factors to $\rho_{\rm core}(\mathbf{G})$ and $\rho_{\rm val}(\mathbf{G})$, thus facilitating the comparison with the model structure factors. The truncated form of Eq. (17a) reads

$$\rho_{\rm val}(\mathbf{r},\mathbf{G}_{\rm max}) = \sum_{\mathbf{G}}^{\mathbf{G}_{\rm max}} \rho_{\rm val}(\mathbf{G}) e^{i\mathbf{G}\cdot\mathbf{r}} \ , \tag{17b}$$

where $\rho_{\rm val}(\mathbf{G})$ is the Fourier transform of $\rho_{\rm val}(\mathbf{r})$ of Eq. (16).

In analogy with Eq. (16) one can partition the free-atom charge densities $n_\alpha(r)$ into core and valence, so that $\rho_{\rm sup}(\mathbf{G})$ in Eq. (14) can be separated accordingly. The difference between the crystalline charge density $\rho_{\rm calc}(\mathbf{r})$ and the reference charge density $\rho_{\rm sup}(\mathbf{r})$ then yields the static deformation density maps

$$\Delta\rho_\mu(\mathbf{r},\mathbf{G}_{\rm max}) = \sum_{\mathbf{G}}^{\mathbf{G}_{\rm max}} [\rho_\mu(\mathbf{G}) - \rho_{{\rm sup},\mu}(\mathbf{G})] e^{i\mathbf{G}\cdot\mathbf{r}} \ , \tag{18}$$

where μ stands for "total," "core," or "valence." The corresponding dynamic deformation density maps $\Delta F(\mathbf{r},\mathbf{G}_{\rm max})$ are obtained by using the dynamic form of $F_{\rm sup}(\mathbf{G})$ [Eq. (15)] and of $F_{\rm calc}(\mathbf{G})$ [Eq. (12a)].

Equations (17b) and (18) depict $\rho_{\rm val}$ and $\Delta\rho$ in a Fourier truncated form. One can use instead the model-density approach of Eq. (7a) to calculate a different approximation to these quantities.[5,6,50] For the valence density one calculates

$$\rho_{{\rm model},v}(\mathbf{r}) = \sum_j \phi(\mathbf{r}-\mathbf{R}_j), \tag{19a}$$

where

$$\phi(\mathbf{r}) = \sum_{nl={\rm val}} \kappa_{nl}^3 \rho_{nl}(\kappa_{nl} r) + R_3(r) K_3(\hat{r}) + R_4(r) K_4(\hat{r}) \tag{19b}$$

and the sum over j in Eq. (19a) extends over unit-cell vectors $\mathbf{R}_j$, while the sum over nl in Eq. (19b) includes only valence orbitals. For the model deformation density map[62]

$$\Delta\rho_{\rm model}(\mathbf{r}) = \rho_{\rm model}(\mathbf{r}) - \rho_{\rm sup}(\mathbf{r}) = \sum_j \Delta\phi(\mathbf{r}-\mathbf{R}_i), \tag{20}$$

where

$$\Delta\phi(\mathbf{r}) = \sum_{nl} [\kappa_{nl}^3 \rho_{nl}(\kappa_{nl} r) - \rho_{nl}(r)] + R_3(r) K_3(\hat{r}) + R_4(r) K_4(\hat{r}) \ . \tag{21}$$

V. DETAILS OF *AB INITIO* CALCULATIONS AND CONVERGENCE

We use the all-electron linearized augmented-plane-wave[63] (LAPW) implementation of the local-density formalism.[8,9] No shape approximation is used in describing the potential and valence charge density, while the core wave functions are obtained self-consistently from the $l = 0$ (spherical) piece of the crystalline potential. We use the Ceperley-Alder[56] exchange correlation functional as parametrized by Perdew and Zunger.[64] The lattice constants used are taken from experiment at the temperature where the x-ray structure-factor measurements were done. They are 3.5670 Å ($T = 298$ K),[44] 5.4307 Å ($T = 295$ K),[30] and 5.6579 Å ($T = 298$ K) (Ref. 45) for C, Si, and Ge, respectively. All calculations are carried out relativistically except for the omission of spin-orbit effects. The latter approximation is rather good: comparison of fully relativistic (with spin orbit) and scalar relativistic (retaining mass-velocity and Darwin effects but omitting spin orbit) calculations for Ge show that the structure factor changed by less than 1 millielectron (me) per atom [or 0.003% for the (111) reflection] in Ge. However, mass-velocity and Darwin effects are important for Ge, as illustrated in Table II.

The great care with which the $F_{\rm expt}(\mathbf{G})$ have been previously measured and analyzed calls for an equivalent assessment of the errors in the calculated counterparts. There are five convergence parameters that control the precision of the LAPW solution[63] to the local-density Hamiltonian: (i) the number $N_{\rm basis}$ of basis functions in which $\psi_i(\mathbf{r})$ are expanded, (ii) the number of $N_{\mathbf{k}}$ of special $\mathbf{k}$ points[65] used in the Brillouin-zone summation of Eq. (9), (iii) the maximum angular momentum $l_{\rm max}$ used in the Kubic harmonic expansion [analogous to Eq. (5)], (iv) the radius $R_{\rm MT}$ of the atomic spheres inside which the Kubic harmonic expansion is taken, and (v) the number $N_{\rm den}$ of Fourier components used to expand the charge density in the interstitial region. We have varied these parameters until an internal convergence to better than a millielectron was obtained.

VI. COMPARISON OF THEORY WITH EXPERIMENT

A. Dynamic and static structure factors of C, Si, and Ge

1. Dynamic structure factors for silicon

Table III gives the measured dynamic Si structure factors $F_{\rm expt}(\mathbf{G})$ and their estimated standard deviation σ.

TABLE III. Dynamic (F) structure factors for Si in units of e/atom corresponding to the most converged set (column 1) in Table I. The experimental data (corrected for anomalous dispersion and nuclear scattering), including the estimated standard deviations σ (in me/atom), are taken from Cummings and Hart (Ref. 1), except the (222) result taken from Alkire, Yelon, and Schneider (Ref. 7). The difference δF_1 is $F_{\rm calc}(\mathbf{G}) - F_{\rm expt}(\mathbf{G})$ (me/atom), while $\delta F_2 = F_{\rm sup}(\mathbf{G}) - F_{\rm expt}(\mathbf{G})$ (me/atom). The root-mean-square deviation for δF_1 is 12 me/atom and an unweighted R factor is 0.21%. The dynamic $F_{\rm calc}(\mathbf{G})$ is obtained from the static $\rho_{\rm calc}(\mathbf{G})$ using $B = 0.4632$ (Ref. 30).

	Dynamic, solid				Dynamic, atoms	
hkl	$F_{\rm calc}(\mathbf{G})$ [Eq. (12a)]	$F_{\rm expt}(\mathbf{G})$ [Eq. (1)]	σ	δF_1	$F_{\rm sup}(\mathbf{G})$ [Eq. (15)]	δF_2
111	10.600	10.6025	2.9	−3	10.455	−148
220	8.397	8.3881	2.2	9	8.450	62
311	7.694	7.6814	1.9	13	7.814	133
222	0.161	0.1820	1.0	−21	0.000	−182
400	6.998	6.9958	1.2	2	7.033	37
331	6.706	6.7264	2.0	−20	6.646	−80
422	6.094	6.1123	2.2	−18	6.077	−35
333	5.760	5.7806	2.1	−21	5.769	−12
511	5.781	5.7906	2.7	−10	5.769	−22
440	5.318	5.3324	2.0	−14	5.302	−30
444	4.115	4.1239	1.8	−9	4.107	−17
551	3.931	3.9349	3.4	−4	3.925	−10
642	3.649	3.6558	5.4	−7	3.644	−12
800	3.253	3.2485	3.4	5	3.251	3
660	2.917	2.9143	1.6	3	2.915	1
555	2.802	2.8009	2.1	1	2.802	1
844	2.165	2.1506	2.4	14	2.163	12
880	1.543	1.5325	2.6	11	1.542	10

This is compared with the local-density calculated structure factors $F_{\rm calc}(\mathbf{G})$ from Eqs. (10) and (12b) [using the best single B value $B = 0.4632$ Å^2 (Ref. 30)]. The difference $\delta F_1 = F_{\rm calc}(\mathbf{G}) - F_{\rm expt}(\mathbf{G})$ is also given. We see that while $|\delta F_1|$ exceeds σ, the largest $|\delta F_1|$ is 21 me/atom and the root-mean-square (rms) deviation over 18 reflections is only 12 me/atom. For some reflections [e.g., (311), (222), (331), and (333)] the difference δF_1 exceeds both calculated and the experimental errors. We suspect that this might reflect a combination of imperfect knowledge of the exchange-correlation functional and uncertainties in the deconvolution of $\rho(\mathbf{G})$ from $F(\mathbf{G})$ [the rigid-atom approximation of Eq. (1)]. The extent of agreement with the data can be measured by the (unweighted) R factor

$$R = \frac{\sum_{\mathbf{G}} ||\rho_{\rm expt}(\mathbf{G})| - |\rho_{\rm calc}(\mathbf{G})||}{\sum_{\mathbf{G}} |\rho_{\rm expt}(\mathbf{G})|} . \quad (22)$$

The present calculation gives for $\{F(\mathbf{G})\}$ $R = 0.21\%$. This represents the best agreement achieved to date between *ab initio* LDA calculated structure factors and experiment. For comparison, Table III also shows the dynamic superposition structure factors $F_{\rm sup}(\mathbf{G})$ [Eq. (15)], where the free-atom densities n_α are calculated also from the local-density formalism using the same exchange correlation as in the crystalline calculation. The deviation from experiment $\delta F_2 = F_{\rm sup}(\mathbf{G}) - F_{\rm expt}(\mathbf{G})$ is significantly larger than $|\delta F_1|$ for $\mathbf{G} < (440)$, hence, solid-state effects are important in this momentum range. While the individual deviations at high $\mathbf{G}$ are small, the difference $F_{\rm calc}(\mathbf{G}) - F_{\rm sup}(\mathbf{G})$ contributed collectively by *all* high-momentum components does add up to affect the shape of $\Delta F(\mathbf{r})$ and $\Delta\rho(\mathbf{r})$, as will be shown below.

We have also calculated $F_{\rm calc}(\mathbf{G})$ using different B values for core and valence densities obtained in the model analysis [Table I (Ref. 6)]. For the first 11 reflections the use of two B values gives an R factor of 0.16%, slightly better than $R = 0.21\%$ obtained with a single B value (Table III). However, there is a systematic deviation as $\mathbf{G}$ increases. The R factor for the full set of 18 reflections is 0.35%, larger than that obtained with a single B value, which remains 0.21%. We conclude that using more than a single B value does not improve the agreement of theory with experiment.

2. *Static structure factors for silicon*

Table IV compares the experimentally deduced static structure factors with theory. We use two different experimentally deduced static structure factors: (a) $\rho_e(\mathbf{G})$, obtained from Eq. (4a) by dividing $F_{\rm expt}(\mathbf{G})$ by a *single* Debye-Waller factor with $B = 0.4632$ Å^2 of Ref. 30 and (b) the model structure factors $\rho_m(\mathbf{G})$ which is the Fourier transform of Eq. (7a) (using two B values obtained in the model fits in Table I). The results are compared to different calculations using various forms of exchange and correlation: the $X\alpha$,[66] Wigner,[67] Hedin-Lunqvist,[68] Singwi *et al.*,[69] Ceperley and Alder,[56] and the weighted-density approximation.[70,71] The table also gives the unweighted R factors of Eq. (22). We see that the agreement between the various theories and

$\rho_e(\mathbf{G})$ is similar to the agreement with $\rho_m(\mathbf{G})$ for the first 11 $\mathbf{G}$ values, for which theoretical results are available. Hence, the use of two different Debye-Waller factors in the model does not significantly affect this comparison. There are, however, systematic deviations between $\rho_m(\mathbf{G})$ and $\rho_e(\mathbf{G})$ for higher $\mathbf{G}$ values: while our R_e value remains 0.21% using either the first 11 $\mathbf{G}$ or all 18 $\mathbf{G}$ values, our R_m increase from 0.16% (11 $\mathbf{G}$ values) to 0.35% (18 $\mathbf{G}$ values).

Our values $R_e = 0.21\%$ and $R_m = 0.16\%$ show improvement over all previous LDA calculations. Note in particular the improvement over the pseudopotential re-

TABLE IV. Comparison between calculated and experimentally deduced static structure factors $\rho(\mathbf{G})$ for Si in units of e/atom. We give two sets of experimental $\rho(\mathbf{G})$: (i) The value $\rho_e(\mathbf{G})$ is extracted from $F_{\text{expt}}(\mathbf{G})$ using in Eq. (4a) a single $B = 0.4632$ from Spackman (Ref. 30). The experimental $F_{\text{expt}}(\mathbf{G})$ (corrected for anomalous dispersion and nuclear scattering) are taken from Cummings and Hart (Ref. 1) except the (222) result taken from Alkire, Yelon, and Schneider (Ref. 7). (ii) The values $\rho_m(\mathbf{G})$ are the Fourier transforms of the static model-density fit by Deutsch (Ref. 6) to the same set of $F_{\text{expt}}(\mathbf{G})$. This uses different B values for core and valence (Table I). In the theoretical values we include only those pseudopotential results in which the core contribution has been added by the authors. We also give the R factors [Eq. (22)] and the number of data points (N) used in comparison. The calculations shown use a variety of approximations for the exchange-correlation potential, i.e., the local-density approximation (LDA) (including the $X\alpha$), the Hartree-Fock (HF) approximation, or the nonlocal weighted-density approximation (WDA). These Hamiltonians were approximately solved by a variety of band-structure methods: LAPW is the linearized augmented plane wave, OPW is the orthogonalized plane wave, LCAO is the linear combination of atomic orbitals, LCGO is the linear combination of Gaussian orbital, and PP is pseudopotential.

hkl $\mathbf{G}$	Expt. $\rho_e(\mathbf{G})$	Expt. $\rho_m(\mathbf{G})$	LAPW[a] (LDA)	LCAO[b] (HF)	OPW[c] ($X\alpha$)	LCAO[d] (LDA)	LCGO[e] (LDA)	PP[f] (LDA)	PP[g] (LDA)	PP[h] (LDA)	LCAO[i] (WDA)
111	10.728	10.713	10.726	10.755	10.70	10.659	10.684	10.691	10.699	10.70	10.522
220	8.656	8.655	8.665	8.640	8.67	8.656	8.630	8.630	8.615	8.57	8.445
311	8.020	8.027	8.033	8.004	8.05	8.068	8.040	7.997	7.976	7.79	8.188
222	0.191	0.181	0.168	0.217	0.17		0.125	0.171	0.170	0.19	0.175
400	7.449	7.454	7.452	7.465	7.49	7.460	7.460	7.415	7.380	7.35	7.505
331	7.247	7.246	7.225	7.269	7.26	7.180	7.191	7.191	7.149	7.03	7.304
422	6.716	6.712	6.696	6.730	6.73	6.683	6.685	6.655	6.610	6.65	6.760
333	6.427	6.420	6.404	6.426	6.41	6.416	6.413	6.357	6.307	6.31	6.534
511	6.438	6.432	6.428	6.459	6.45	6.417	6.421	6.385	6.336	6.35	
440	6.046	6.033	6.030	6.060	6.07		6.020		5.940	6.00	5.970
444	4.979	4.952	4.968	4.983	5.04						
551	4.807	4.783	4.802	4.815							
642	4.555	4.521	4.546	4.556							
800	4.176	4.149	4.182	4.187							
660	3.866	3.834	3.870	3.871							
555	3.760	3.728	3.761	3.758							
844	3.135	3.114	3.155	3.147							
880	2.533	2.509	2.551	2.536							
R_e%			0.21	0.24	0.38	0.42	0.46	0.62	1.09	1.44	1.53
R_m%			0.16	0.36	0.39	0.35	0.36	0.56	1.02	1.40	1.47
N			11	11	11	8	10	9	10	9	

[a]Present LAPW results, using the Perdew-Zunger parametrized Ceperley-Alder LDA exchange-correlation (XC) potential and 60 special $\mathbf{k}$ points in the Brillouin-zone integrations.

[b]Reference 28, using the self-consistent LCAO Hartree-Fock method and a Gaussian-type of orbitals. The results quoted here were calculated using an 8–41G** basis set, which yields the lowest total energy.

[c]References 20 and 21, using a six $\mathbf{k}$ points nonrelativistic self-consistent OPW calculated valence charge density with the $X\alpha$ ($\alpha = \frac{2}{3}$) potential (Ref. 66), to which a core charge density was added from relativistic free-atom Hartree-Fock data.

[d]Reference 23, using the self-consistent LCAO method and the $X\alpha$ ($\alpha = \frac{2}{3}$) potential, with 19 $\mathbf{k}$ points in the Brillouin-zone integrations.

[e]Reference 22, using the self-consistent LCGO method and the Wigner XC potential (Ref. 67) with ten special $\mathbf{k}$ points in the Brillouin-zone integrations.

[f]Reference 19, using the self-consistent plane-wave pseudopotential method with a basis-set cutoff of 24 Ry and the Wigner potential with ten special $\mathbf{k}$ points in the Brillouin-zone summation.

[g]Reference 18, using the plane-wave pseudopotential method with a basis-set cutoff of 11.5 Ry and Wigner XC potential with ten special $\mathbf{k}$ points in the Brillouin-zone summation.

[h]Reference 15, using the mixed-basis pseudopotential method and exchange ($\alpha = \frac{2}{3}$) plus the Singwi *et al.* correlation potential (Ref. 69), with ten special $\mathbf{k}$ points in the Brillouin-zone integrations.

[i]Reference 29, using a LCAO description of the bond charge and a nonlocal weighted-density approximation (WDA) (Ref. 70) to exchange correlation (Ref. 71), with six high-symmetry $\mathbf{k}$ points in the Brillouin-zone integrations.

sults, e.g., Yin and Cohen[18] giving $R_e = 1.09\%$ and $R_m = 1.02\%$, Zunger[16] yielding $R_e = 1.44\%$ and $R_m = 1.40\%$, and the improvement over the recent weighted-density calculation of Balbás *et al.*[29] $R_e = 1.53\%$ and $R_m = 1.47\%$. The recent Hartree-Fock calculation of Pisani, Dovesi, and Orlando[28] yields a rather good $R_e = 0.24\%$ and $R_m = 0.36\%$.

The improvement in the present calculation over previous *pseudopotential* results reflects our use of an all-electron representation whereby core and valence states are treated self-consistently as solid-state wave functions on equal footing. The improvement in the present calculation over previous *all-electron* results stems primarily from a better formulation of the expansions of wave functions and potentials, permitting more effective convergence. That the improvement is *not* due to the choice of the correlation functional can be seen by repeating our LAPW calculations with different correlation functionals. We find for the 11 reflections of Table IV the (R_e, R_m) error factors of (0.21,0.16); (0.22, 0.17); (0.26,0.17), and (0.27,0.18) using the Ceperley-Alder,[56] Hedin-Lunqvist,[68] Wigner,[67] and the $X\alpha$ (with $\alpha = \frac{2}{3}$) (Ref. 66) exchange correlation, respectively. Also, the improvement of the present calculation over the older calculation cannot be attributed to the increased speed and storage of present-day computers, since a complete Si calculation with better than 1 millielectron error takes only 3 min on a CRAY YMP; even with a 20-fold slower machine this calculation is still affordable.

3. *Dynamic structure factors for diamond*

Table V compares the calculated dynamic $F_{\rm calc}(\mathbf{G})$ with the experimental $F_{\rm expt}(\mathbf{G})$ values. We have calculated $F_{\rm calc}(\mathbf{G})$ from Eq. (12b) using the appropriate Debye-Waller factors (Table I): $B = 0.1379$ Å^2 for the TTKS data and $B = 0.2303$ Å^2 for comparing with the GW data. The differences $\delta F_1 = F_{\rm calc}(\mathbf{G}) - F_{\rm expt}(\mathbf{G})$ are larger than those seen in Si: the rms deviation is 17 me/atom and the R factor for $\{F(\mathbf{G})\}$ is 0.94% for the TTKS data. For the GW data, the rms deviation for δF_1 is 31 me/atom and $R = 2.25\%$. Clearly, *ab initio* theory agrees with the TTKS data much better than with the

TABLE V. Dynamic (F) structure factors for diamond in units of e/atom. We show two sets of experimental data: the single-crystal results of Takama *et al.* (TTKS) (Ref. 39) except the (222) reflection which are taken from Weiss and Middleton (Ref. 37), and the powder data of Göttlicher and Wölfel (GW) (Ref. 36). σ denotes the estimated standard deviation in the data (in me/atom). The calculated values $F_{\rm calc}(\mathbf{G})$ are obtained from Eq. (4a) using the Debye-Waller factor B appropriate to each experimental data set: $B = 0.1379$ Å^2 for TTKS and $B = 0.2303$ Å^2 for GW (see Table I). The difference δF_1 is $F_{\rm calc}(\mathbf{G}) - F_{\rm expt}(\mathbf{G})$ (me/atom). The root-mean-square deviation for δF_1 of TTKS is 17 me/atom and the unweighted R factor is 0.94%. For GW, we find the rms for δF_1 is 31 me/atom and $R = 2.25\%$.

	TTKS data				GW data			
hkl	$F_{\rm calc}(\mathbf{G})$	$F_{\rm expt}(\mathbf{G})$	σ	δF_1	$F_{\rm calc}(\mathbf{G})$	$F_{\rm expt}(\mathbf{G})$	σ	δF_1
111	3.256	3.247	11	9	3.238	3.311	7	−73
220	1.934	1.920	5	14	1.906	1.912	9	−6
311	1.650	1.648	4	2	1.618	1.586	7	32
222	0.108	0.144	10	−36	0.105	0.108	10	−3
400	1.498	1.491	6	7	1.455	1.379	9	76
331	1.480	1.483	7	−3	1.429	1.456	5	−27
422	1.344	1.363	10	−19	1.286	1.301	2	−15
333	1.268	1.287	5	−19	1.208	1.263	5	−55
511	1.286	1.310	2	−24	1.225	1.263	5	−38
440	1.207	1.198	3	9	1.139	1.120	9	19
531	1.155				1.084	1.090	3	−6
620	1.086				1.010	1.027	5	−17
533	1.053				0.974	0.989	5	−15
444	0.984				0.902			
551	0.950				0.866	0.876	3	−10
711	0.946				0.863	0.876	3	−13
642	0.892				0.806	0.824	3	−18
553	0.858				0.771	0.788	8	−17
731	0.861				0.773	0.788	8	−15
800	0.810				0.721			
733	0.782				0.692			
660	0.739				0.648	0.674	4	−26
822	0.738				0.648	0.674	4	−26
555	0.715				0.624	0.639	6	−15
751	0.713				0.623	0.639	6	−16
753	0.653				0.562	0.582	4	−20
911	0.652				0.561	0.582	4	−21

GW data. We also notice that the scaled GW structure factors are systematically larger than the calculated values by an average of 17 me/atom for $\mathbf{G} \geq (531)$.

4. Static structure factors for diamond

There are many previous calculations of the *static* structure factors[21,72–77] and charge-density maps[13,78–86] of diamond. Table VI compares the experimental static $\rho_{\text{expt}}(\mathbf{G})$ deduced from the TTKS and the GW data with various previous theoretical calculated values.[21,72–77] Since for diamond $B_{\text{core}} = B_{\text{valence}}$ (Table I), there is no ambiguity in the choice of $\rho_e(\mathbf{G})$ vs $\rho_m(\mathbf{G})$ as discussed for Si. Hence, the experimental $\rho_{\text{expt}}(\mathbf{G})$ were obtained from Eq. (4a) by using a single Debye-Waller factor from Table I. As was the case for the dynamic structure factors, we find that all calculations agree much better with the TTKS data than with the GW data. The $X\alpha$ calculation of Ivey[72] produces the best R factor ($R_1 = 0.80\%$ and $R_2 = 1.91\%$), while our calculation yields $R_1 = 0.95\%$ and $R_2 = 2.36\%$. Our R factor for the static structure factors in diamond is ~ 5 times larger than our R factor for Si (0.21%). This is partly due to the fact that the denominator of R for diamond is only $\frac{1}{3}$ that of Si, even though the rms value of δF_1 is only slightly larger than that of Si (for the TTKS data).

5. Dynamic structure factors for germanium

Table VII compares the experimental $F_{\text{expt}}(\mathbf{G})$ of Ge with the calculated values using $B = 0.5654$ Å^2 obtained in the relativistic fit (Table I). The rms error between theory and experiment is 170 me/atom and the R factor is 0.85%. Solid-state effects are apparent by noting that the R factor of $F_{\text{expt}}(\mathbf{G})$ relative to the superposition of free atom density is 1.10%.

6. Static structure factors for germanium

Table VIII compares various theoretically calculated static $\rho_{\text{calc}}(\mathbf{G})$ with experiment. We use two experimental sets of ρ_{expt}: one derived from a model fit using Clementi's *nonrelativistic* Hartree-Fock free-atom structure factors, and one using *relativistic* LDA orbitals in the fit (see Table I). We see that the relativistic model fit produces consistently better R values: $R_R = 0.43\%$ and $R_{\text{NR}} = 0.58\%$. Both values are relatively small, owing to the larger denominator $[\sum |\rho_{\text{expt}}(\mathbf{G})|]$ for Ge and the two scaling factors in the fit (Table I), even though the rms of $|\Delta F_1|$ (170 meV/atom) is more than 14 times larger than that of Si (12 meV/atom). Our results and the OPW calculation of Raccah *et al.*[21] produce the lowest R factors.

TABLE VI. Comparison between calculated and experimentally deduced static structure factors $\rho(\mathbf{G})$ for diamond in units of e/atom. We show two sets of experimental $\rho(\mathbf{G})$: The value $\rho_1(\mathbf{G})$ is extracted from $F_{\text{expt}}(\mathbf{G})$ of TTKS using in Eq. (4a) $B = 0.1379$ Å^2. The value $\rho_2(\mathbf{G})$ is extracted from $F_{\text{expt}}(\mathbf{G})$ of GW using in Eq. (4a) $B = 0.2303$ Å^2. We show the corresponding R factors of two data sets relative to different calculations. N is the number of reflections used to calculate R. See the caption to Table IV for the definitions of the calculation methods used.

hkl	Expt.		LAPW[a]	SCPWG[b]	LCAO[c]	LCGO[d]	LCAO[e]	OPW[f]	LCAO[g]
$\mathbf{G}$	$\rho_1(\mathbf{G})$	$\rho_2(\mathbf{G})$	LDA	$X\alpha$	$X\alpha$	HF	HF	$X\alpha$	$X\alpha$
111	3.274	3.357	3.282	3.290	3.273	3.249	3.274	3.33	3.349
220	1.962	1.982	1.976	1.966	1.992	1.960	1.925	1.97	2.023
311	1.697	1.667	1.700	1.690	1.720	1.693	1.659	1.66	1.748
222	0.149	0.114	0.111	0.117	0.137	0.070	0.088	0.14	0.075
400	1.557	1.483	1.564	1.570	1.494	1.543	1.535	1.53	1.590
331	1.562	1.587	1.558	1.570	1.600	1.526	1.533	1.55	1.564
422	1.454	1.451	1.434	1.451	1.423	1.427	1.443	1.42	1.452
333	1.385	1.427	1.364	1.398	1.381	1.376	1.382	1.34	1.394
511	1.409	1.427	1.384	1.398	1.385	1.381	1.386	1.37	1.401
440	1.306	1.294	1.316	1.325				1.31	
R_1%			0.95	0.80	1.56	1.55	1.55	1.72	2.18
R_2%			2.36	1.91	2.14	3.05	2.58	2.20	2.48
N			10	10	9	9	9	10	9

[a]Present LAPW results, using the Perdew-Zunger parametrized Ceperley-Alder exchange-correlation (XC) potential with ten special $\mathbf{k}$ points in the Brillouin-zone integrations.

[b]Reference 72, using the self-consistent mixed-basis plane wave plus Gaussian (SCPWG) method and the $X\alpha$ ($\alpha = 0.758\,47$) potential, with six high-symmetry points in the Brillouin-zone integrations.

[c]Reference 74, using a self-consistent LCAO method and exchange-only potential with ten special $\mathbf{k}$ points in the Brillouin-zone integrations.

[d]Reference 75, using a minimum basis-set Gaussian-orbital Hartree-Fock method.

[e]Reference 76, using the self-consistent LCAO Hartree-Fock method with a minimum basis set of Slater-type orbitals.

[f]Reference 21, using a self-consistent OPW method and the $X\alpha$ ($\alpha = 1$) potential with four $\mathbf{k}$ points in the Brillouin-zone integrations.

[g]Reference 77, the results were obtained using a self-consistent LCAO method and $X\alpha$ ($\alpha = 1$) potential with 19 $\mathbf{k}$ points in the Brillouin-zone integrations.

7. "Forbidden" reflections in C, Si, and Ge

The model of superposition of spherically symmetric atomic charge densities [Eq. (15)] produces $F_{\rm sup}(\mathbf{G}) = 0$ for the reflections $\mathbf{G}$ for which $h+k+l = 4n \pm 2$, where n is an integer. This defines the (pseudo) "forbidden" reflections, e.g., (222) and (442) and (622), (644), and (842). (Note, however, that if $h+k+l = 4n \pm 2$ *and* any one of the three indices h, k, or l is zero, then the reflection is *strictly* forbidden for the diamond structure.) Of course, the actual charge density is deformed from spherically symmetric densities due to bonding effects, so, in reality, the pseudoforbidden reflections carry a finite (although weak) intensity. Within the multipole expansion framework of our model, the finite structure factors for the quasiforbidden reflections are due to two effects. The first is due to the existence of an antisymmetric, odd-l, bonding component in the static charge density in Eq. (5). The second is due to anharmonic thermal motion (finite β), which exists in the centrosymmetric charge density [all even l components in Eq. (5)].

Since the intensities of the forbidden reflections are smaller by two orders of magnitude or more than the allowed ones their accurate measurement is an extremely demanding task. Thus, only the lowest-order reflections, (222), (442), and (622), were ever measured.[58,59] The importance of these reflections stems from the fact that their intensity is determined solely by the small effects of anharmonicity and bond deformation, whereas for the allowed reflections these small contributions are completely masked by the much larger spherical charge contributions. Furthermore, since the deformation densities are part of the valence shell, they can provide information on postulated nonrigid thermal motion of the atom, where the valence shell moves with a different Debye-Waller factor than the core.[6,87] Their measured values have been therefore employed repeatedly to test the quality of model fits and *ab initio* calculations of the crystalline charge distribution. In particular, they provide stringent tests for the derived values of β, valence-shell

TABLE VII. Dynamic (F) structure factors for Ge in units of e/atom. The experimental data $F_{\rm expt}(\mathbf{G})$ (corrected for the thermal motion and anomalous dispersion) are from the MK (Ref. 40) and DHC (Ref. 43) data sets. The dynamic $F_{\rm calc}(\mathbf{G})$ are obtained from static $\rho_{\rm calc}(\mathbf{G})$ by using $B = 0.5654$ (see Table I). The difference δF_1 is $F_{\rm calc}(\mathbf{G}) - F_{\rm expt}(\mathbf{G})$ (me/atom), while $\delta F_2 = F_{\rm sup}(\mathbf{G}) - F_{\rm expt}(\mathbf{G})$ (me/atom). The root-mean-square deviation for δF_1 is 170 me/atom and the unweighted R factor is 0.86%.

	Dynamic, solid			Dynamic, atoms		
hkl $\mathbf{G}$	$F_{\rm calc}(\mathbf{G})$ [Eq. (12a)]	$F_{\rm expt}(\mathbf{G})$ [Eq. (1)]	σ	δF_1	$F_{\rm sup}(\mathbf{G})$ [Eq. (15)]	δF_2
111	27.156	27.292[a]	60	−136	27.042	−250
111	27.156	27.541[b]	52	−385	27.042	−499
220	22.861	22.688[a]	50	173	22.927	239
311	21.121	20.919[a]	60	202	21.234	315
222	0.114	0.131[a]	10	−17	0	−131
400	18.932	18.667[a]	53	265	18.976	309
331	17.868	17.823[a]	71	45	17.839	16
422	16.204	16.041[a]	53	163	16.194	153
333	15.333	15.192[a]	90	141	15.327	135
333	15.333	15.383[b]	15	−50	15.327	−56
511	15.332				15.327	
440	14.054	13.855[a]	53	199	14.041	186
531	13.363				13.352	
620	12.325				12.317	
533	11.761				11.757	
444	10.916	10.977[b]	24	−61	10.910	−67
551	10.451				10.448	
711	10.453				10.448	
642	9.749				9.745	
553	9.366				9.360	
731	9.362				9.360	
800	8.773				8.771	
733	8.449				8.447	
660	7.949				7.948	
822	7.949				7.948	
555	7.672	7.695[b]	17	−23	7.672	−23
751	7.673				7.672	
777	3.942	3.930[b]	10	12	3.946	16

[a]Reference 40.
[b]Reference 43.

TABLE VIII. Comparison between calculated and the experimentally deduced static structure factors $\rho(\mathbf{G})$ for Ge in units of e/atom. The experimental data $\rho_{\text{expt}}(\mathbf{G})$ (corrected for the thermal motion and the anomalous dispersion) are the Fourier transforms of the static model-density fit to the observed MK and DHC data sets. We give both the fit to the scalar-relativistic LDA (SR-LDA) atomic data and to the nonrelativistic Hartree-Fock (NR-HF) atomic data. The R factor for the LAPW (for all 12 measured data) are $R_{\text{SR}} = 0.37\%$ and $R_{\text{NR}} = 0.62\%$.

hkl	Expt.		LAPW[a]	OPW[b]	LCGO[c]	LCAO[d]
G	SR-LDA	NR-HF	LDA	$X\alpha$	LDA	WDA
111	27.894	28.009	27.519	27.54	27.457	27.181
220	23.766	23.839	23.683	23.63	23.615	23.615
311	22.142	22.208	22.172	22.07	22.125	22.189
222	0.152	0.143	0.120	0.24	0.110	0.185
400	20.235	20.286	20.318	20.27	20.280	20.395
331	19.482	19.531	19.432	19.47	19.368	19.622
422	18.040	18.072	18.016	18.00	17.955	18.145
333	17.300	17.323	17.275	17.21	17.218	17.352
511			17.273	17.24	17.218	
440	16.198	16.199	16.187	16.16	16.115	16.155
444	13.498	13.450	13.493			
555	10.680	10.593	10.684			
777	7.547	7.461	7.543			
$R_{\text{SR}}\%$			0.43	0.52	0.64	0.87
$R_{\text{NR}}\%$			0.58	0.73	0.83	0.88
N			9	9	9	9

[a]Present LAPW results, using the Perdew-Zunger parametrized Ceperley-Alder exchange-correlation (XC) potential with ten special **k** points in the Brillouin-zone integration.

[b]Reference 21, using a self-consistent OPW method and the $X\alpha$ ($\alpha = \frac{2}{3}$) potential with four **k** points in the Brillouin-zone integration.

[c]Reference 22, using the LCGO method and Wigner potential with ten special **k** points in the Brillouin-zone integration.

[d]Reference 29, using a LCAO description of the bond-charge model and weighted-density approximation (WDA) potential with six high-symmetry **k** points in the Brillouin-zone integration.

Debye-Waller parameter, and, to a lesser extent, the deformation density.

The measured, model-fitted, and LDA-calculated structure factors for the first three forbidden reflections are given in Table IX. Note that while the measured F_{222} were included in the model fits (so their model value is not a prediction), F_{442} and F_{622} were not, and are used only to test the accuracy of the model and the *ab initio* calculations. The table shows a good overall agreement of both model and LDA values with the measurements.[7,36,37,39,40,58,59,88,89] The model values are all within 10 me at most of the measured ones. The *ab initio* values deviate somewhat more, the maximal deviation being ~ 35 me for F_{222} of diamond. The deviations for most reflections, however, are similar to those of the model. The LDA results are consistently smaller than the model fitted values. For germanium, the only case for which the fit yields $\beta \neq 0$, this is not surprising, since the LDA calculations, unlike the model, use $\beta = 0$. To examine these effects we calculate the forbidden reflections of Ge assuming in the fit $\beta = 0$. The $\beta = 0$ model values listed in Table IX for germanium indeed show a much better agreement with the LDA results, although, as expected, they deviate more from the measured results, thus indicating that anharmonic effects are significant in this case. For germanium, relativistic effects may be expected to be large enough to be observed. Indeed, the use of relativistic free-atom scattering amplitudes in the model fits improves the agreement with experiment significantly. However, an accurate assessment of these relativistic effects will have to await a more accurate, and more complete body of measured structure factors than available now.

Finally, the good agreement of the model and measured forbidden structure factors lends credence to the conclusions drawn from the model fits here and in Ref. 6, i.e., (i) $\beta \approx 0$ and 1 eV/Å^3 for silicon and germanium, respectively, (ii) shell-dependent thermal motion in silicon having $B_{\text{core}} \neq B_{\text{valence}}$, (iii) the $2sp$ and $3sp$ shell expansion in silicon, and (iv) the valence-shell expansion in germanium.

B. Untruncated core, valence, and total static charge densities

Having established the level of accuracy of the calculated $F(\mathbf{G})$ and $\rho(\mathbf{G})$ over the limited set of momenta accessible to high-precision measurements, we next consider the calculated real-space charge densities *without* any Fourier truncation. Recall that the basis set used in our LAPW calculation includes real-space orbitals that contain arbitrarily large momentum components. Figure 1 depicts the calculated $\rho_{\text{val}}(\mathbf{r})$ [Eq. (9)],

while Figs. 2–4 show the *deformation* charge densities $\Delta\rho_{\rm core}(\mathbf{r})$, $\Delta\rho_{\rm val}(\mathbf{r})$, and $\Delta\rho_{\rm tot}(\mathbf{r})$, respectively [Eq. (18) for $\mathbf{G} \to \infty$]. In this and in the subsequent figures we show side-by-side line plots in the $\langle 111 \rangle$ direction and contour plots in the (110) plane. The solid squares denote atomic positions, empty triangles denote the (empty) tetrahedral interstitial sites, while the empty half diamond symbols at the left and right margins denote the (empty) hexagonal interstitial sites. Distances are given in terms of the fraction of $\sqrt{3}a$, where a is the lattice constant. The origin is on the left atom. The bond center is at $x = 0.125$. Contour step values are given in the insets. The basic features are as follows.

(i) As expected intuitively, the core charge density $\rho_{\rm core}(\mathbf{r})$ is localized around the nuclei. However, the core is not entirely inert: the core deformation density $\Delta\rho_{\rm core}(\mathbf{r})$ (Fig. 2) is slightly *negative* in the core region. This effect is naturally missed by all "frozen-core" and by pseudopotential calculations.

(ii) The valence charge density $\rho_{\rm val}(\mathbf{r})$ [Fig. 1] exhibits the following features: (a) *maxima* on the atomic sites, (b) the lobes on the bonds are oriented *parallel* to the $\langle 111 \rangle$ bond direction, (c) there is a local *minimum* at the bond center [point δ in Fig. 1(a)], flanked by two local maxima (point γ), and (d) there is charge *accumulation* in the the back-bond region (point α). These characteristics are reversed when one considers the valence *deformation* charge density $\Delta\rho_{\rm val}(\mathbf{r})$ for Si and Ge (Fig. 3): Now there are *minima* on the atomic sites, the lobes on the bonds are oriented *perpendicular* to the bond direction (in Si and Ge but not in C), there is a *maximum* at the bond center [point δ in Fig. 3(a)], and charge depletion in the back-bond region α. Table X gives the positions R_i (in units of $\sqrt{3}a$ with origin on the leftmost atom)

TABLE IX. Measured, model, and LAPW-calculated $F(\mathbf{G})$ values for the "forbidden" reflections $h+k+l = 4n \pm 2$. All values are in millielectron units. The model fits are defined in Table I. The LAPW results assume $\beta = 0$.

	β	F_{222}	F_{442}	F_{622}
		Diamond		
Model:				
TTKS fit	0.0	136.8		
GW fit	0.0	107.9		
LAPW:				
$B = 0.1379$	0.0	107.6	8.3	2.7
$B = 0.2303$	0.0	105.3	7.7	2.5
Expt.[a]	0.0	143.8		
		Silicon		
Model:	0.0	180.8	11.2	3.1
LAPW:	0.0	160.5	7.9	1.7
Expt.:				
AYS[b]		182.0		
TB1[c]	3.45		4.38	
MB[d]	3.38		5.25	0.63
TB2[e]	3.38		4.63	1.10
		Germanium		
Model:				
NR fit[f]	1.81	141.3	17.1	9.4
NR fit $\beta = 0$	0.0	136.1	4.2	1.0
R fit[g]	0.88	146.6	11.6	5.6
R fit $\beta = 0$	0.0	143.8	4.8	1.2
LAPW: $B = 0.5654$	0.0	113.5	2.6	2.0
Expt.:				
MK[h]		133.0		
MB[d]	1.32		7.88	6.98
TB2[e]	1.27		12.29	8.25

[a]Reference 37.
[b]Reference 7.
[c]Reference 88.
[d]Reference 89.
[e]Reference 58. For β see Ref. 45.
[f]Using *nonrelativistic* free-atom form factors of Ref. 51.
[g]Using *relativistic* LDA free-atom form factors calculated by us.
[h]Reference 40.

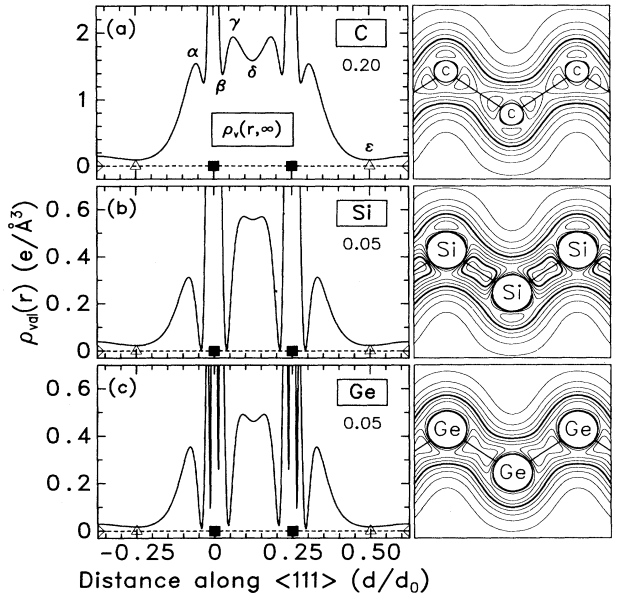

FIG. 1. Calculated untruncated ($\mathbf{G} \to \infty$) valence charge densities $\rho_{\rm val}(\mathbf{r})$ [Eq. (17a)] for (a) diamond, (b) Si, and (c) Ge. In this and in the subsequent figures we show side-by-side line plots in the ⟨111⟩ direction and contour plots in the (110) plane. The solid squares denote atomic positions, empty triangles denote the (empty) tetrahedral interstitial sites, while the empty half-diamond symbols at the left and right margins denote the (empty) hexagonal interstitial sites. Distances are given in terms of the fraction of $\sqrt{3}a$, where a is the lattice constant. The origin is on the leftmost atom. The bond center is at $x = 0.125$. The insets denote contour steps $e/\text{Å}^3$. The outmost contour has the same values as the contour steps. The values of the prominent features (the points α, β, γ, δ, and ϵ) are listed in Table X.

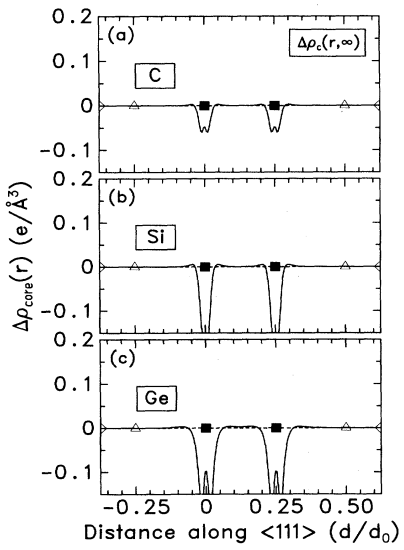

FIG. 2. Calculated untruncated ($\mathbf{G} \to \infty$) static core deformation charge densities $\Delta\rho_{\rm core}(\mathbf{r})$ [Eq. (18)] for (a) C (diamond), (b) Si, and (c) Ge. Note that the core is not fully inert but that the fluctuation $\Delta\rho_{\rm core}$ is localized.

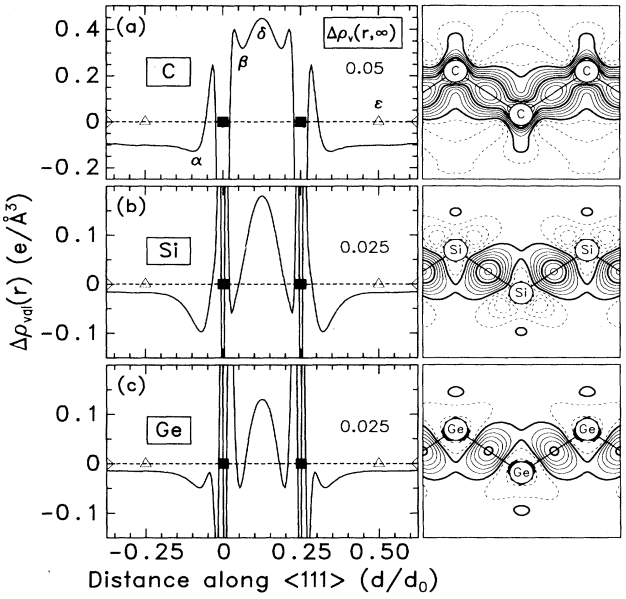

FIG. 3. Calculated untruncated ($\mathbf{G} \to \infty$) static valence deformation charge densities $\Delta\rho_{\rm val}(\mathbf{r})$ [Eq. (18)] for (a) diamond, (b) Si, and (c) Ge. The thick outer solid contour next to the dashed line denotes $\Delta\rho = 0$. Dashed contours denote negative $\Delta\rho$. The insets denote contour steps in units of $e/\text{Å}^3$. The $\Delta\rho$ values of the prominent features (the points α, β, and δ) are listed in Table XI. Note that the bond charge is elongated parallel to the bond direction in diamond while in Si and Ge it is perpendicular to the bond direction.

and amplitude $\rho_{\rm val}(R_i)$ of these features $i = \alpha$, β, γ, δ, and ϵ for C, Si, and Ge, while Table XI gives similar results for the deformation valence density $\Delta\rho_{\rm val}(R_i)$. Both tables compare the *ab initio* values with those deduced through our model from experiments. We see that the amplitude of the local extremum of $\rho_{\rm val}$ and $\Delta\rho_{\rm val}$ at the bond-center point (δ) decreases rapidly in the sequence C→Si→Ge (largely a volume effect), as does the charge density at the tetrahedral interstitial site (point ϵ). There are interesting differences between diamond on the one hand and Si and Ge on the other: both $\rho_{\rm val}$ and $\Delta\rho_{\rm val}$ are bond oriented in C, whereas $\Delta\rho_{\rm val}$ in Si and Ge are oriented perpendicular to the bond direction. Furthermore, Si and Ge exhibit deep minima on either side of the "camel's back" bond charge [point β in Fig. 1(a)], whereas these minima are considerably shallower in diamond (Table X). The significant difference between $\rho_{\rm val}$ and $\Delta\rho_{\rm val}$ (including a factor of ~ 3 reduction in overall amplitude) suggests that many of the features of $\rho_{\rm val}$ are dominated by contributions from the free atoms.

(iii) Since most of the peaked amplitude of $\rho_{\rm core}(\mathbf{r})$ is localized inside the core region, $\Delta\rho_{\rm val}$ (Fig. 3) and $\Delta\rho_{\rm tot}$ (Fig. 4) are similar over most of the unit-cell space. This is seen also from the last four lines of Table X, where the locations and amplitudes of the main features of $\Delta\rho_{\rm val}$ and $\Delta\rho_{\rm tot}$ are compared.

(iv) The total charge density $\rho_{\rm tot}$ is dominated by the core contribution and, as is expected, lacks structure. The amplitude $\rho_{\rm tot}(R_\delta)$ at the bond-center point δ is

TABLE X. Values of the valence and total charge density [$\rho_{\rm val}(R)$ and $\rho_{\rm tot}(R)$ in $e/\text{Å}^3$] and $|R|$ (in units of $\sqrt{3}a$, origin on the left atom) at various points (α, β, γ, δ, and ϵ) along the $\langle 111\rangle$ direction as indicated in Figs. 2 and 3. The second line for each entry lists the corresponding value obtained from the model fits to the measured structure factors. The negative $\rho_{\rm val}$ value obtained for Ge from the model at point ϵ gives an idea of the uncertainty in the model fit. We only list the model fit of TTKS data for diamond.

	C		Si		Ge	
	ρ	$\|R\|$	ρ	$\|R\|$	ρ	$\|R\|$
			$\rho_{\rm val}(R_\alpha)$			
Calc.	1.55	0.056	0.31	0.081	0.36	0.077
Expt.	1.47	0.060	0.30	0.083	0.40	0.079
			$\rho_{\rm val}(R_\beta)$			
Calc.	1.38	0.029	0.01	0.040	0.02	0.044
Expt.	1.08	0.030	0.13	0.042	0.16	0.042
			$\rho_{\rm val}(R_\gamma)$			
Calc.	1.94	0.064	0.57	0.096	0.49	0.091
Expt.	1.93	0.069	0.58	0.103	0.60	0.092
			$\rho_{\rm val}(R_\delta)$			
Calc.	1.59	0.125	0.56	0.125	0.46	0.125
Expt.	1.61	0.125	0.58	0.125	0.58	0.125
			$\rho_{\rm val}(R_\epsilon)$			
Calc.	0.09	0.50	0.02	0.50	0.02	0.50
Expt.	0.10	0.50	0.02	0.50	−0.01	0.50
			$\rho_{\rm tot}(R_\delta)$			
Calc.	1.59	0.125	0.56	0.125	0.49	0.125
Expt.	1.61	0.125	0.58	0.125	0.61	0.125

TABLE XI. Values of the $\Delta\rho_{\rm val}(R)$ and $\Delta\rho_{\rm tot}(R)$ ($e/\text{Å}^3$) and $|R|$ (in units of $\sqrt{3}a$, origin on the left atom) at various points (α, β, and δ) along the $\langle 111\rangle$ direction as indicated in Figs. 5 and 6. The second line for each entry lists the corresponding values obtained from the model fits to the measured structure factors. Entries left blank indicate the absence of the corresponding features in the model. We use the TTKS data for the diamond model.

	C		Si		Ge	
	$\Delta\rho$	$\|R\|$	$\Delta\rho$	$\|R\|$	$\Delta\rho$	$\|R\|$
			$\Delta\rho_{\rm val}(R_\alpha)$			
Calc.	−0.13	0.097	−0.10	0.071	−0.05	0.077
Expt.	−0.21	0.098	−0.10	0.071	−0.01	0.068
			$\Delta\rho_{\rm tot}(R_\alpha)$			
Calc.	−0.13	0.097	−0.10	0.072	−0.05	0.076
Expt.	−0.21	0.098	−0.10	0.075	−0.01	0.068
			$\Delta\rho_{\rm val}(R_\beta)$			
Calc.	0.32	0.062	−0.06	0.027	−0.05	0.053
Expt.			0.05	0.056	0.09	0.057
			$\Delta\rho_{\rm tot}(R_\beta)$			
Calc.	0.32	0.063	−0.09	0.024	−0.06	0.051
Expt.			0.06	0.061	0.09	0.057
			$\Delta\rho_{\rm val}(R_\delta)$			
Calc.	0.45	0.125	0.18	0.125	0.13	0.125
Expt.	0.45	0.125	0.20	0.125	0.25	0.125
			$\Delta\rho_{\rm tot}(R_\delta)$			
Calc.	0.45	0.125	0.18	0.125	0.13	0.125
Expt.	0.45	0.125	0.20	0.125	0.25	0.125
			$\Delta\rho_{\rm val}(R_\epsilon)$			
Calc.	−0.10	0.50	−0.02	0.50	−0.02	0.50
Expt.	−0.07	0.50	−0.02	0.50	−0.05	0.50
			$\Delta\rho_{\rm tot}(R_\epsilon)$			
Calc.	−0.10	0.50	−0.02	0.50	−0.02	0.50
Expt.	−0.07	0.50	−0.02	0.50	−0.05	0.50

close to the amplitude of $\rho_{\rm val}(R_\delta)$, indicating that the core contribution is negligible there.

(v) The deformation density maps $\Delta\rho_{\rm tot}$ (Fig. 4) and $\Delta\rho_{\rm val}$ (Fig. 3) have sharp nodal features near the core and sharp minima in the "inner-bond region" (point β in Figs. 3 and 4), both reflecting the fact that upon formation of the solid from the atoms the nodes in the crystal valence wave functions are shifted with respect to those in the free-atom valence orbitals. As will be shown below, the representation of these sharp features will require relatively high-momentum components in a Fourier description.

C. Comparison of all-electron and pseudopotential valence charge density

The pseudopotential approximation has proven to be extremely successful in many solid-state calculations[90] as it enables the replacement of the quantum-mechanical interference effects of core wave functions with an effective, semiclassical external potential, which is computationally far more expedient. The resulting pseudo-wave-functions can be made nodeless and smooth by an appropriate choice of this external (pseudo)potential. Comparison with measured structure factors requires, however, the reintroduction of (i) core orbitals and (ii) core-valence orthogonality corrections. Current procedures for implementing this are often based on adding to the calculated solid-state *valence* charge density the *free-atom core* densities (hence, neglecting $\Delta\rho_{\rm core}$ of Fig. 2). This includes approximately effect (i) but neglects effect (ii) (although core orthogonalization is possible for certain classes of pseudopotentials, see Ref. 15 for details). Table IV indeed shows that the agreement of the corrected pseudopotential $\rho_{\rm calc}(\mathbf{G})$ values with experiment is mediocre. However, the valence pseudo-charge-density is generally very close to the valence density component of all-electron calculations. This is illustrated in Fig. 5, which shows the pseudopotential results of Martins and Zunger[91] and can be compared to the current all-electron results shown in Fig. 1. There is a remarkable agreement between the two sets of calculations outside the core region. Of course, the maxima on the atoms and the dip β are absent in the pseudopotential description.

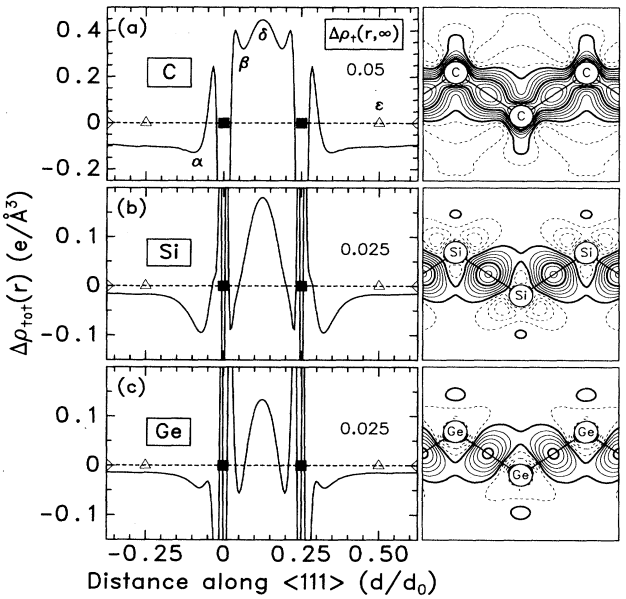

FIG. 4. Calculated untruncated ($\mathbf{G} \to \infty$) static total deformation charge densities $\Delta\rho_{\rm tot}(\mathbf{r})$ [Eq. (18)] for (a) diamond, (b) Si, and (c) Ge. The thick outer solid contour next to the dashed line denotes $\Delta\rho = 0$. Dashed contours denote negative $\Delta\rho$. The insets denote contour steps in units of $e/\text{Å}^3$. The values at the prominent features (the points α, β, and δ) are listed in Table XI. Note that like in Fig. 3 the bond charge is elongated parallel to the bond direction in diamond while in Si and Ge it is perpendicular to the bond direction.

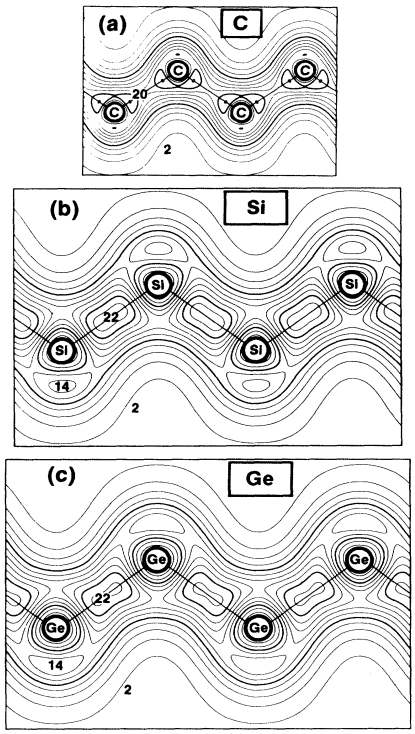

FIG. 5. Pseudopotential valence charge densities of (a) diamond, (b) silicon, and (c) germanium from Martins and Zunger (Ref. 91). The density is given in units of e/cell (not $e/\text{Å}^3$). Contour steps is $2e$/cell. Note the close similarity to the all-electron results (contour plots in Fig. 1) outside the core regions.

D. Fourier-truncated charge-density maps for Si

Given that even *deformation* charge-density maps exhibit rather sharp features in $\mathbf{r}$ space, we next examine the convergence of their Fourier representation. Figure 6 shows the calculated Si deformation density $\Delta\rho_{\rm tot}(\mathbf{r}, \mathbf{G}_{\rm max})$ of Eq. (18) for three sets of $\mathbf{G}$ vectors. First [Fig. 6(a)] we use calculated $\rho_{\rm calc}(\mathbf{G})$ at the set of $\mathbf{G}$ vectors of Cummings and Hart (Table III), em-

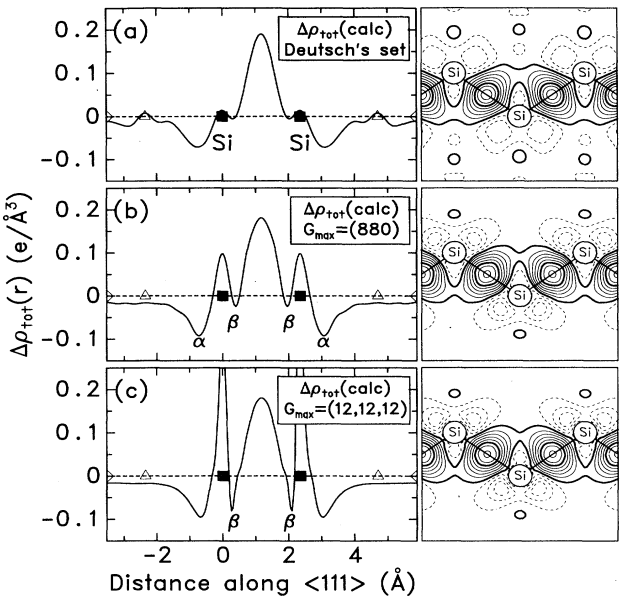

FIG. 6. Convergence of the *ab initio* calculated static deformation charge density $\Delta\rho(\mathbf{r}, \mathbf{G}_{\max})$ [Eq. (18)] of Si with respect to the maximum momentum $\mathbf{G}_{\max}$ included in the Fourier series (denoted in the inset): (a) The Cummings-Hart-Deutsch set of $\mathbf{G}$ vectors (Table III); (b) all reflections up to $\mathbf{G}_{\max} = (880)$, and (c) all reflections up to $\mathbf{G}_{\text{big}} = (12, 12, 12)$ (288 $\mathbf{G}$ components). Contour step = $0.025e/\text{Å}^3$. Dashed contours denote negative $\Delta\rho$. Note that (c) is practically identical to the untruncated $\Delta\rho(\mathbf{r}, \infty)$ of Fig. 4(b). Note further that the set of reflections used in (a) is able to capture the details of the converged charge in the bond region but misses the localized features β and the amplitude of the charge density on the atomic sites.

ployed also by Deutsch in his analysis. While this set extends to $\mathbf{G} \leq (880)$, it includes only 18 of the 52 allowed reflections contained in this range. Second [Fig. 6(b)] we show $\Delta\rho_{\text{tot}}$ calculated from all 52 reflections up to $\mathbf{G}_{\max} = (880)$. Finally [Fig. 6(c)] we depict $\Delta\rho_{\text{tot}}$ for $\mathbf{G}_{\text{big}} = (12, 12, 12)$ (288 $\mathbf{G}$ components), outside the range of current high-precision measurements. The latter $\Delta\rho$ plot closely resembles the untruncated $\Delta\rho_{\text{tot}}(\mathbf{r}, \infty)$ of Fig. 4(b) (except for the inner-core region). The evolution of $\Delta\rho_{\text{tot}}(\mathbf{r}, \mathbf{G}_{\max})$ with $\mathbf{G}_{\max}$ seen in Fig. 6 clearly exhibits robustness of the amplitude near the bond center. At the same time, the amplitudes on the (a) atomic site, (b) inner-bond minima β, (c) back-bond minima α, and (d) the tetrahedral interstitial sites are far from convergence using Deutsch's set of 18 $\mathbf{G}$ vectors. This slow convergence of $\Delta\rho(\mathbf{r}, \mathbf{G}_{\max})$ with $\mathbf{G}_{\max}$ reflects the modification of the core of bonded atoms relative to free atoms [see Eq. (18)]. Interestingly, Fig. 6 shows that $\Delta\rho(\mathbf{r}, \mathbf{G}_{\max})$ does not contain noisy undulation for any level of truncation $\mathbf{G}_{\max}$. This disproves the assertion of Zuo, Spence, and O'Keefe[33] that adding terms in a Fourier series for $\Delta\rho$ beyond about the first ten only adds noise.

Figure 7 shows similar information for the *valence* density: it depicts the evolution of $\rho_{\text{val}}(\mathbf{r}, \mathbf{G}_{\max})$ with the highest value of $\mathbf{G}_{\max}$ (indicated in the insets) included in the Fourier series of the type of Eq. (11). One sees a transition from a smooth behavior at low $\mathbf{G}_{\max}$ [Fig. 7(a)] to an oscillatory function at intermediate $\mathbf{G}_{\max}$ values [Figs. 7(c)–7(e)] and finally to a smooth function at high $\mathbf{G}_{\max}$ values [Fig. 7(f)]. The latter Fourier-synthesized function is nearly indistinguishable from the real-space representation $\rho_{\text{val}}(\mathbf{r}, \infty)$ of Fig. 1(b). Like Fig. 6, Fig. 7 also shows the insufficiency of the Cummings-Hart-Deutsch set in capturing the full structure of the converged charge density if it is described by a Fourier series. Hence, despite the high precision of the individual structure factors of Cummings and Hart, the set of $\mathbf{G}$ vectors included in them is insufficient to represent the full details of $\rho_{\text{val}}(\mathbf{r})$ or $\Delta\rho_{\text{tot}}(\mathbf{r})$ when used to Fourier synthesize the electron density.

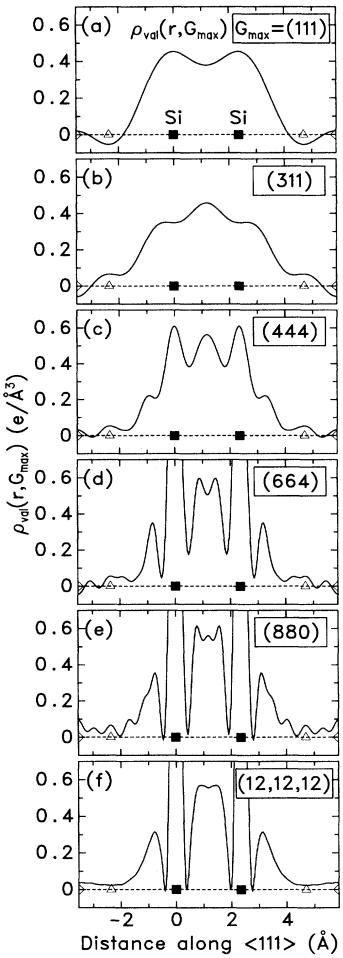

FIG. 7. Convergence of the *ab initio* calculated static valence density $\rho_{\text{val}}(\mathbf{r}, \mathbf{G}_{\max})$ [Eq. (17b)] of Si with respect to the highest momentum included in the Fourier sum (denoted in the insets). Note that (f) is practically identical to the untruncated $\rho_{\text{val}}(\mathbf{r}, \infty)$ of Fig. 1(b). Note further that as $\mathbf{G}_{\max}$ increases ρ_{val} changes from a smooth function [in (a)] to an oscillatory function [(c)–(e)] and finally to a smooth function (f). Even the set $\mathbf{G}_{\max} \leq (880)$ (the best that can be measured to date) is insufficient to produce a smooth ρ_{val}.

E. Comparison of *ab initio* and model charge densities: $\rho_{\rm val}$

The text surrounding Eqs. (4b)–(7a) highlights the fundamental difference between a Fourier-synthesis approach [Eq. (4b), illustrated in Figs. 6 and 7] and the model-density approach [Eqs. (5)–(7a)] of Dawson,[46] Stewart,[47,48] Coppens,[49] Spackman,[30,44] and Deutsch:[5,6] the latter method is guaranteed, by construction, to yield a smooth function despite the use of a limited set of structure factors. We will next compare the results of the model density to our *fully converged* results.

1. $\rho_{\rm val}$ *in silicon*

Figure 8 compares our calculated $\rho_{\rm val}(\mathbf{r},\infty)$ [Eq. (17a)] for silicon with Deutsch's model valence density [Eq. (19a), see parameters in Table I (Ref. 92)]. The agreement between theory and the experimentally derived function is excellent. Table X gives a quantitative comparison of ρ_v(calc) and ρ_v(model) at locations α, β, γ, δ, and ϵ of Fig. 8. The only significant discrepancy exists in the inner-bond minima (point β), where our result shows a significantly lower amplitude than Deutsch's fit. Figure 6 demonstrated, however, that this feature is highly dependent on Fourier truncation. Our results and those of Deutsch are very different from the elliptic, single-peaked density obtained by Yang and Coppens[93] using a truncated Fourier series.

2. $\rho_{\rm val}$ *in diamond*

Figure 9 compares the *ab initio* calculated valence density map [part (a)] with the model-density result [Eq. (19)] using the fits to the TTKS and the GW data [solid and dashed lines in part (b)]. The agreement of theory with experiment is fair. Table X gives a quantitative comparison at some points. Our *ab initio* $\rho_{\rm val}$ at points α, γ, and δ [Fig. 9(a)] are 1.55, 1.94, and 1.59e/Å^3, which are close to the values 1.47, 1.93, and 1.61, respectively obtained from fitting the TTKS data and values 1.66, 2.06, and 1.61, respectively, obtained from fitting the GW data.

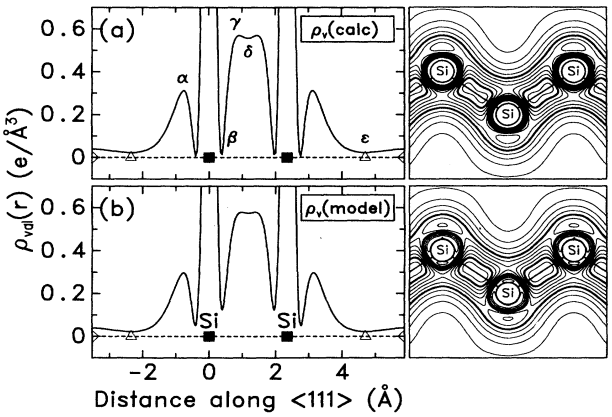

FIG. 8. Comparison of the *ab initio* calculated static valence charge density $\rho_{\rm val}$ of Si [Eq. (17a)] with Deutsch's fit to the data of Cummings and Hart (b). The contour step is 0.05e/Å^3. See text for quantitative comparisons.

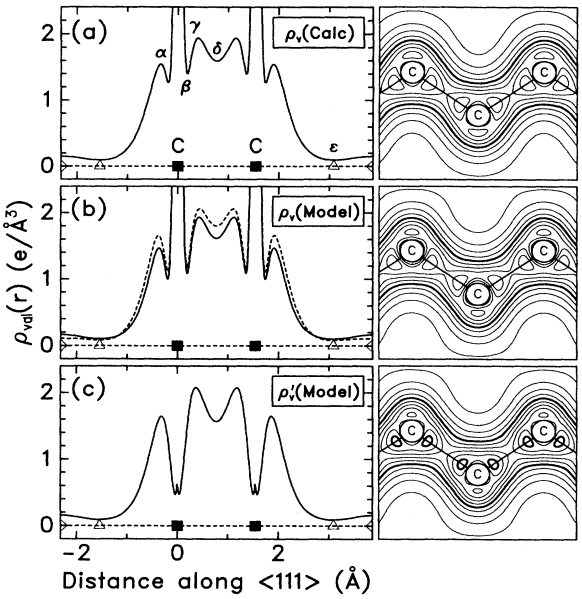

FIG. 9. Comparison of the *ab initio* calculated static valence charge density (a) $\rho_{\rm val}$ [Eq. (17a)] of diamond with (b) the model density from fitting the TTKS data (solid line) and GW data (dashed line). The corresponding contour plot is for the TTKS data. Part (c) shows Spackman's results (Ref. 44) in which Stewart's orbital for 2s and Clementi's orbital for 2p are used. The contour step is 0.20e/Å^3. See the text for quantitative comparisons.

It can be seen from Eq. (19) that the shape of $\rho_{{\rm model},v}$ at the nuclear sites depends sensitively on the choice of atomic-orbital densities n_{nl} since $R_{l\neq 0}(r=0)=0$, see Eq. (6). We have consistently used for these quantities Clementi's[51] Hartree-Fock data. Spackman used for n_{2s} Stewart's density-localized value[52] while for n_{2p} he used Clementi's values.[51] The quality of the fit of $F_{\rm expt}(\mathbf{G})$ is the same whether one uses Clementi's orbitals or Stewart's unitarily rotated orbitals. However, the *components* of the charge density depend on the choice of orbital basis in the fit. Figure 9(c) shows the model density $\rho'_{\rm val}$ using Stewarts orbitals in the fit. Comparison with Fig. 9(b) shows significant differences between these model valence densities near the atomic sites: Spackman's fit [Fig. 9(c)] gives *local minima* at the atomic sites, while ours [Fig. 9(b)] produces *maxima* on the atomic sites. Except at the atomic sites, which are expected to depend strongly on the nature of the orbitals employed, the two models are in fairly good agreement. The theoretical calculations in Fig. 9(a) clearly agree better with our model in Fig. 9(b).

3. $\rho_{\rm val}$ *in germanium*

Figure 10 compares our *ab initio* valence density of Ge [part (a)] with the result from the model fit using rela-

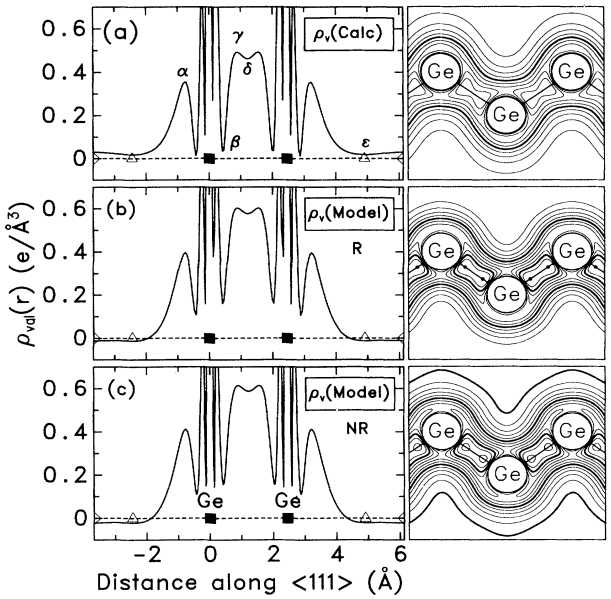

FIG. 10. Comparison of the *ab initio* calculated static valence charge density (a) $\rho_{\rm val}$ [Eq. (17a)] of germanium with the (b) and (c) model density. Part (b) shows the model fit using relativistic (R) orbital, while part (c) shows the model fit using nonrelativistic (NR) orbitals. The contour step is $0.05e/\text{Å}^3$.

tivistic [part (b)] and nonrelativistic orbitals [part (c)] in the fit. Table X shows a quantitative comparison at some points. The overall shapes of ρ_v(calc) and ρ_v(model) are very similar. The small negative portions of ρ_v(model) near the interstitial sites (see also Table X) are unphysical. They probably reflect a too high $F_{\rm expt}(111)$ value. These negative regions have, however, a much smaller amplitude (by a factor of 2) in the relativistic fit when compared with the nonrelativistic fit. As a result of the negative segments of ρ_v(model) in the interstitial sites, the normalization of ρ_v(model) in the other regions must be too high. Indeed, the model values are higher than the *ab initio* value at the bond regions (points γ and δ, see Table X). Clearly, better experimental data are needed for Ge before a definitive model can be adopted and compared with theory.

4. *The bond-centered local minimum in* $\rho_{\rm val}$

Figures 8, 9, and 10 show that the valence charge densities of Si, C, and Ge all exhibit local minimum along the ⟨111⟩ bond axes. This feature is very pronounced in diamond; however, its subtlety in Si and Ge led to much debate in the theoretical literature. We now know from experiment that this feature is real. Many early pseudopotential calculations on silicon seem to have missed this feature, e.g., Walter and Cohen,[10] Chelikowsky and Cohen,[11] Ihm and Cohen,[17] Yin and Cohen,[18(a)] Hamann,[14] Zunger and Cohen,[15] and Denteneer and van Haeringen.[81] More recent pseudopotential calculations (using more accurate pseudopotential and better converged calculations) have predicted the local minima in the valence density, e.g., Martins and Zunger[91] (see Fig. 5), Yin and Cohen,[18(b)] van Camp, van Doren, and Devreese,[82] and Nielsen and Martin.[19] All-electron calculations have also observed the local minimum, e.g., Pisani, Dovesi, and Orlando,[28] Methfessel, Rodriguez, and Andersen,[25] Polatoglou and Methfessel,[26] and Weyrich.[24] None of the previous calculation on Ge, except that of Martins and Zunger[91] (Fig. 5), seem to have found a local minimum in the valence density.

F. Comparison of *ab initio* and model charge densities: $\Delta\rho_{\rm tot}$

1. *Deformation maps for silicon*

Figure 11(a) compares our *ab initio* calculated deformation charge density of $\Delta\rho_{\rm tot}$ [Eq. (18) for $\mathbf{G}\to\infty$] for Si with the model density. Table XI gives a quantitative comparison at some points. The overall shapes are similar: $\rho_{\rm tot}$ is perpendicular to the bond, has a bond-center maximum (point δ) and a minimum at the back-bond position α, and a shallow negative value in the interstitial sites. The shape near the atoms (point β) [best seen in the line plot of Fig. 11(b)] are, however, significantly different. The model shows sharp peaks at the β points with pronounced minima on the atomic sites. These features are unmatched by any Fourier synthesis (Fig. 6) and may reflect the difficulty in reproducing the complexity of a realistic $\Delta\rho_{\rm tot}$ within the arbitrary restricted representation for $R_l(r)$ used in Dawson's model [Eqs. (6a) and (6b)]. It is remarkable, however, that despite the clear insufficiency of the Cummings-Hart-Deutsch set of momenta to describe $\rho_{\rm val}$ or $\Delta\rho_{\rm tot}$ in a *Fourier representation* (see Figs. 6 and 7), the *model-density* approach of Eqs. (5)–(7a) mimics very well the overall results obtained from a highly converged Fourier series.

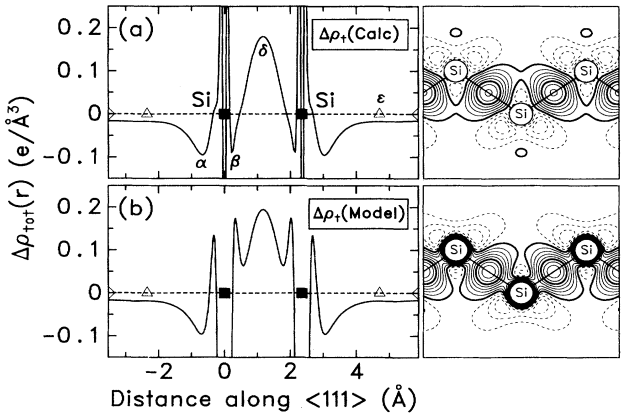

FIG. 11. Comparison of the experimentally deduced static density deformation plots $\Delta\rho_{\rm tot}(\mathbf{r})$ [Eq. (18)] of Si (b) with our *ab initio* calculation (a). The contour step is $0.025e/\text{Å}^3$. Dashed contours denote negative $\Delta\rho$.

2. *Deformation maps for diamond*

Figure 12 compares the *ab initio* calculated static density deformation map $\Delta\rho_{\rm tot}(\mathbf{r})$ [Eq. (18)] of diamond (a) with two experimentally deduced static density deformation plots: that obtained from the TTKS data [Fig. 12(b)] and from the GW data [Fig. 12(c)]. Table XI gives a quantitative comparison between the *ab initio* result and model $\Delta\rho$ extracted from the TTKS data. The overall agreement is considerably better with the TTKS data, as noticed also in comparing calculated and measured structure factors (Sec. VI A 3). Notice in particular that the amplitude of the GW results are too high at the bond center, and that $\Delta\rho$ in this model has the wrong slope in the interstitial region. The shapes near the atomic sites are very different in the two model densities. This deserves further comment: we see from Eq. (21) that if the orbital deformation parameter κ_{nl} is 1, $\Delta\phi$ is given just by the $l \neq 0$ terms $R_3K_3 + R_4K_4$. The conventional functional choice of $R_l(r)$ is such that $R_{l\neq 0}(r = 0) = 0$ [Eq. (6)]. Hence, this choice *forces* $\Delta\phi(\mathbf{r})$ to have zero amplitude on the nuclei. On superposing $\Delta\phi$ over unit cells [Eq. (20)] one finds some amplitude on the atomic sites. These amplitudes result only from the penetration of the tails of $R_l(r)$ from sites $i \neq j$ onto site j. This choice of a restrictive functional flexibility of $R_{l\neq 0}(r)$ limits its ability to capture fluctuations at the nuclear sites. Figure 6 further illustrates that the amplitude of $\Delta\rho(\mathbf{r})$ on the nuclear sites develops only when high $\mathbf{G}$ components are included. The GW data set, having higher $\mathbf{G}$ components than the TTKS set, shows indeed more structure near the atomic sites. We conclude that the currently used model-density approach [with $\kappa_{nl} = 1$ and $R_{l\neq 0}(r = 0) = 0$] lacks sufficient functional flexibility to resolve the structure of $\Delta\rho$ near the nuclei.

3. *Deformation maps for germanium*

Figure 13 compares our *ab initio* calculated $\Delta\rho(\mathbf{r})$ of Ge with the results of the model fit using relativistic [part (b)] and nonrelativistic [part (c)] orbitals in the fit. We see that relativistic effects change the bond-elongated $\Delta\rho$ [Fig. 13(c)] to a more spherically shaped bond $\Delta\rho$ [Fig. 13(b)] in much better agreement with the theory [Fig. 13(a)]. Furthermore, the dips denoted by α and β in the theoretical density plot along the bond in Fig. 13(a) show up only in the relativistic model fit, but not in the nonrelativistic one. Their positions also agree rather well with those of the model. All these indicate that relativistic effects have significant contributions to the electronic density of crystalline germanium.

G. Subjecting the Si *ab initio* results to model fits

Another way of comparing the *ab initio* results with the experimentally deduced model values is to subject both sets of structure factors to the same model analysis. One then fits the set of *calculated* static structure factors $\{\rho_{\rm calc}(\mathbf{G})\}$ by the model (naturally, with $\beta = B = 0$) and obtains the fit parameters $\{\kappa_{nl}, A_l, \xi\}$ of Eqs. (5) and (6), which can be compared with those obtained by fitting the

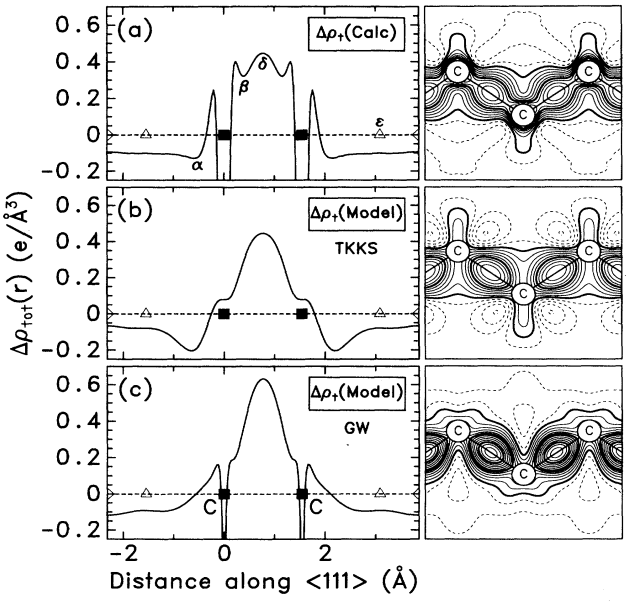

FIG. 12. Comparison of the *ab initio* calculated static density deformation plots $\Delta\rho_{\rm tot}(\mathbf{r})$ [Eq. (18)] of diamond (a) and the experimentally deduced static density deformation plots of TTKS (b) and GW (c). The contour step is $0.05e/\text{Å}^3$. Dashed contours denote negative $\Delta\rho$.

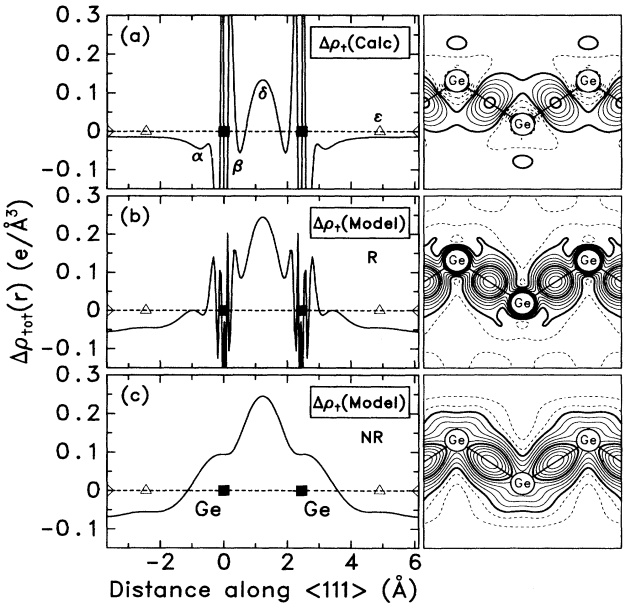

FIG. 13. Comparison of the *ab initio* calculated static deformation charge density (a) $\rho_{\rm val}$ [Eq. (17a)] of germanium with the (b) and (c) model density. Part (b) shows the model fit using the relativistic (R) orbital, while part (c) shows the model fit using nonrelativistic (NR) orbitals. The contour step is $0.025e/\text{Å}^3$.

$\{F_{\rm expt}(\mathbf{G})\}$ to the same model. The interest in this procedure stems from the fact that it subjects both sets of structure factors—calculated and measured—to the *same* analysis. Any restriction in the model (e.g., limited functional flexibility near the nuclei) will be equally reflected in both fits. Note that $\rho_{\rm calc}(\mathbf{G})$ has no $\mathbf{G}$-dependent systematic deviations from the measured values where those are available. We will assume that the $\rho_{\rm calc}(\mathbf{G})$ continue to be accurate also for the high-order structure factors which are at present outside the reach of accurate experiment. (This is reasonable since the higher-order terms increasingly reflect core contributions.) One can, therefore, monitor the results of the fit of $\rho_{\rm calc}(\mathbf{G})$ as a function of $\mathbf{G}_{\rm max}$. This allows one to separate model-dependent features from those depending on the accuracy of the "measured" set of structure factors.

Figure 14 shows how the parameters ξ, A_3, A_4, and $\kappa_{\rm val}$ [Eq. (6)], deduced from fitting $\rho_{\rm calc}(\mathbf{G})$ of Si to the model, depend on the number of calculated structure factors used in the fit. The curves in Fig. 14 converge after about 120 terms to their limiting values of $\xi = 2.806$ a.u.$^{-1}$, $A_3 = 0.266e$, and $A_4 = -0.062e$. We see that as $\mathbf{G}_{\rm max}$ is increased (i) the exponent ξ *increases* (i.e., the radial charge density becomes more localized), (ii) the coefficient A_3 *decreases* (i.e., the antisymmetric component of the charge density diminishes), and (iii) A_4 becomes less negative (i.e., a lower centrosymmetric charge component). Similarly, (iv) $\kappa_{\rm val}$, starting out at small $\mathbf{G}_{\rm max}$ as $\kappa_{\rm val} < 1$ (orbital expansion) increases, and turns to $\kappa_{\rm val} > 1$ (orbital contraction) at higher $\mathbf{G}_{\rm max}$ values. The converged orbital deformation parameters using a large number of $\rho_{\rm calc}(\mathbf{G})$ values are $\kappa_{\rm core}(n = 2) = 1.0003$, and $\kappa_{\rm val} = 1.0124$, as compared to the experimental values deduced from the 18 known structure factors $\kappa_{\rm core}(n = 2) = 0.9949$, and $\kappa_{\rm val} = 0.9382$. It is possible, therefore, that a model fit to a more complete set of measured structure factors will yield a vanishing expansion of the $2sp$ shell, and a small ($\sim$1%) *contraction* of the valence shell, rather than the values found in the model, fits to a set of 18 reflections. (v) Limiting the fit to the 11 structure factors for which theory versus experiment comparison exists (Table IV), we find an R factor of 0.079%, i.e., about half of what was found for LAPW versus the experimental model fit.

(vi) Finally, we made also a series of fits to the calculated structure factors including in the model two more terms of the multipole expansion, i.e., $l = 0, 3, 4, 6, 7$ in Eq. (7a). No improvement was observed in the statistical indices of the fits, and no significant variations were detected in the derived parameter values, as compared with the $l = 0, 3, 4$ term fits. This is in good agreement with identical observations for fits to the canonical set of the 18 measured structure factors.

Figure 15 shows the model static valence density along the ⟨111⟩ direction for (a) the fit to the 18 *experimental* $F_{\rm expt}(\mathbf{G})$ values, (b) the fit to the set of 18 *calculated* $\rho_{\rm calc}(\mathbf{G})$ values, and (c) the fit to the 288 *calculated* $\rho_{\rm calc}(\mathbf{G})$ values. In all three cases, one first fits $\rho(\mathbf{G})$ to the model, then uses the fitted model parameters to construct the crystal density [Eq. (7) and Fig. 15]. One sees remarkable agreement between Figs. 15(a) and 15(b) as well as with the density shown in Fig. 7(f) obtained with

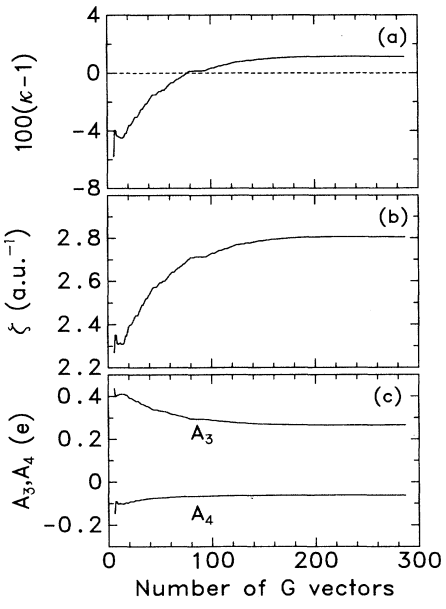

FIG. 14. The variation of the Si model fitting parameters: (a) valence expansion or contraction coefficient κ, (b) coefficient ξ of Eq. (6b), and (c) octupole and hexadecapole terms A_3 and A_4 with the number of $\mathbf{G}$ values included in the fit. The structure factors fitted are static LAPW values.

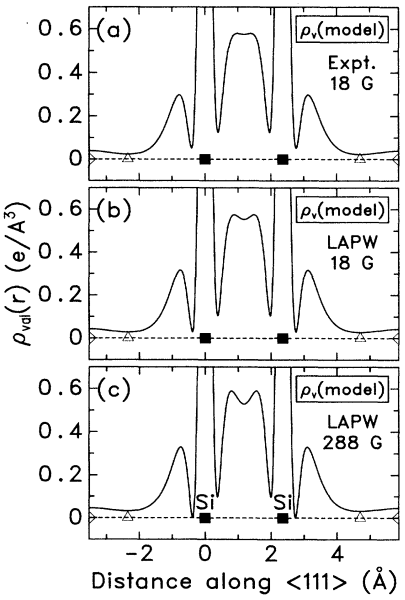

FIG. 15. This figure gives the model valence charge density along the ⟨111⟩ direction by subjecting both the experimental and LAPW structure factors to the same model. (a) The fit to the 18 experimental $F_{\rm expt}(\mathbf{G})$, (b) the fit to a set of 18 calculated $\rho_{\rm calc}(\mathbf{G})$ values, and (c) the fit to the $\mathbf{G}_{\rm big} = (12, 12, 12)$ (288 $\mathbf{G}$ components) calculated $\rho_{\rm calc}(\mathbf{G})$ values.

a Fourier series (but no fit). In contrast, Fig. 15(c) is significantly different. This means that: (i) if one uses *a large set* of structure factors, the accurate result obtained by Fourier summation [Fig. 7(f)] is different from that obtained from the model fit [Fig. 15(c)]. In other words, there is a loss of information in fitting a structure factor set with high-**G** components to Dawson's model. This is related to the limited functional flexibility of the model near the core, discussed above, and is evidenced by the large fitting error we find in Fig. 15(c). (ii) If one uses *a smaller set* of structure factors, a direct Fourier series produces noise [Fig. 7(e)], while fitting it to the model [Fig. 15(b)] filters out the noise. This reflects the fact that Dawson's model extrapolates the high-**G** components using a spatially smooth form. (iii) It follows from (i) and (ii) above that when a limited set of structure factors is available experimentally, the best strategy is to fit it to Dawson's model (rather than Fourier sum it directly). To compare the resulting $\rho_v(\mathbf{r})$ with theory, one should either subject an equivalently small set of $\rho_{\rm calc}(\mathbf{G})$ to a model fit [Figs. 15(a) and 15(b)] or Fourier sum a *converged* set of $\rho_{\rm calc}(\mathbf{G})$ [Fig. 7(f)]. Subjecting a large set of $\rho(\mathbf{G})$ to a model fit or subjecting a small set of $\rho(\mathbf{G})$ to Fourier summation both produce significant errors.

H. Static versus dynamic deformation densities

The differences near the nuclei between the model-density approach and *ab initio* calculations for the *static* deformation maps (Figs. 11–13) suggest that perhaps *dynamic* effects need to be considered. Zuo, Spence, and O'Keeffe[33] conjectured that while high-momentum Fourier components could affect the shape of the static deformation densities $\Delta\rho_{\rm tot}(\mathbf{r},\mathbf{G}_{\rm max})$, they would be inconsequential for the dynamic deformation density $\Delta F_{\rm tot}(\mathbf{r},\mathbf{G}_{\rm max})$, since the Debye-Waller factors would effectively attenuate such high-**G** components. This suggested to them the pessimistic conclusion[33] that one cannot recover any information on high-order $\rho_{\rm expt}(\mathbf{G})$ terms from a deconvolution [Eq. (4a)] of $F_{\rm expt}(\mathbf{G})$. To test this hypothesis we plotted in Fig. 16 the static $\Delta\rho_{\rm tot}(\mathbf{r},\mathbf{G}_{\rm max})$ [Eq. (18)] and the dynamic $\Delta F_{\rm tot}(\mathbf{r},\mathbf{G}_{\rm max})$ [from Eq. (13)] for two truncations: $\mathbf{G}_{\rm max}=(331)$ [Figs. 16(a) and 16(b)] and $\mathbf{G}_{\rm big}=(12,12,12)$ (288 **G** components) [Figs. 16(c) and 16(d)]. This shows that (i) the shapes of $\Delta\rho(\mathbf{r},\mathbf{G}_{\rm max})$ depend on $\mathbf{G}_{\rm max}$ in this range. Both $\Delta\rho(\mathbf{r})$ and $\Delta F(\mathbf{r})$ are affected by this truncation, and (ii) $\Delta\rho_{\rm tot}\cong\Delta F_{\rm tot}$ at any of these truncations except that a reduction of the amplitude on the nuclei is evident. This invalidates the conjecture of Zuo, Spence, and O'Keefe.[33] Clearly, the Debye-Waller factor $\exp(-G^2B)$ does not decay fast enough to render a high-order contribution to $\Delta\rho(\mathbf{G})$ negligible.

The similarity of $\Delta\rho_{\rm calc}(\mathbf{r},\mathbf{G}_{\rm max})$ to $\Delta F_{\rm calc}(\mathbf{r},\mathbf{G}_{\rm max})$ over much of the unit-cell volume implies that (i) the difficulty in calculating *ab initio* dynamic charge densities can be effectively circumvented for many purposes by using the far simpler static densities. (ii) Since high-momentum Fourier components $F(\mathbf{G}_{\rm big})$ clearly affect

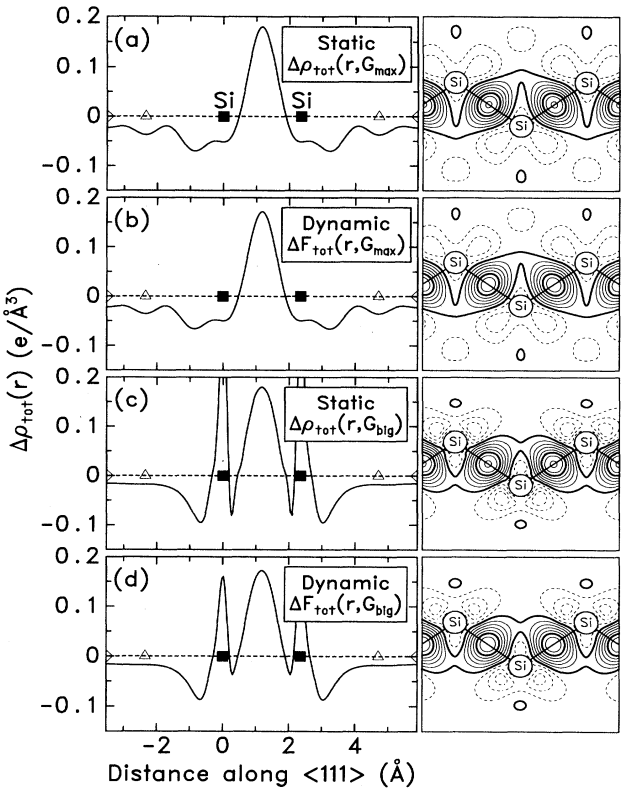

FIG. 16. Comparison of static ($\Delta\rho$) and dynamic (ΔF) total deformation density maps of Si for two Fourier truncations: $\mathbf{G}_{\rm max}=(331)$ in (a) and (b), and $\mathbf{G}_{\rm big}=(12,12,12)$ (288 **G** components) in (c) and (d). The contour step is $0.025e/\text{Å}^3$. Dashed contours denote negative values. Note the similarity of the static and dynamic maps for the same $\mathbf{G}_{\rm max}$ and the lack of convergence of $\Delta\rho$ and ΔF for $\mathbf{G}_{\rm max}\leq(330)$.

charge-density deformation plots (viz., Fig. 6) and valence charge-density plots (viz., Fig. 7), the current inability to measure $F(\mathbf{G}_{\rm big})$ with high precision poses a real limitation to our ability to accurately characterize $\Delta\rho_{\rm tot}(\mathbf{r})$.

VII. SUMMARY AND CONCLUSIONS

(i) *Model fits.* The multipole expansion formalism with the lowest-order centrosymmetric and antisymmetric terms ($l=0,3,4$) accounts well for the measured structure factors. Fits of the model to both silicon and germanium yield a goodness of fit of $\sim$1, exhausting the accuracy of the available data. For diamond, the only high-accuracy set available to date yields a goodness of fit of $\sim$4. Further progress awaits more accurate measurements for germanium, and the extension of the small set of structure factors available for both diamond and germanium. The much better and more complete set of structure factors available for silicon could nevertheless be improved by accurate measurements of high-order structure factors.

(ii) *Features observed in the fits.* The charge distribution in silicon and germanium are similar in general, and

differ from that of diamond. The following features are observed. (a) A valence-shell expansion of a few percent is found in silicon and germanium, but not in diamond. (b) An ~0.5% expansion of the core $2sp$ shell of silicon. (c) Both the octupole ($l = 3$) and hexadecapole ($l = 4$) terms are populated in silicon and germanium, but only the octupole is populated in diamond. (d) Nonrigid thermal motion with different Debye-Waller factors was found in silicon, but not in the other two crystals. The silicon valence charge exhibits a much reduced thermal vibrational amplitude, as compared to the core. (e) Relativistic effects are noticeable for germanium even at the present 20–30-millielectron level of experimental accuracy. (f) No evidence for an anharmonic term in the effective potential was found for silicon and diamond. For germanium, by contrast, the fits indicate the existence of a small but non-negligible anharmonic term.

(iii) *Structure factors.* Precise implementation of the local-density theory is able to reproduce all accurately measured Si structure factors with a maximum error of ~ 20 me/atom and often considerably better. R factors for 18 reflections are as small as 0.21% and the rms deviation is 12 me/atom. The agreement with the currently available data for C and Ge is poorer (an R factor of 0.94% for C and 1.05% for Ge, respectively, and the rms deviations are 17 me/atom and 170 me/atom for C and Ge, respectively). This reflects largely the inferior quality of the C and Ge data relative to the Si data.

(iv) *Valence and deformation densities.* The valence charge density $\rho_{\rm val}(\mathbf{r})$ extracted from experiment are accurately reproduced by the local-density theory (Figs. 8–10 and Table X). While the features of the deformation densities are well reproduced in the bond regions (Figs. 11–13 and Table XI), the shapes near the atomic sites are not. We suspect that this reflects a limitation in the choice of a simple radial function [Eqs. (6a) and (6b)] in the model fit to experiment.

(v) *Trends in calculated* $\rho_{\rm val}$ *and* $\Delta\rho_{\rm tot}$. Valence density maps $\rho_v(\mathbf{r})$ (Fig. 1) exhibit a camel's back double-maximum structure on the bond in C, Si, and Ge. It is more pronounced in C and Ge than in Si (note the nonmonotonic trend here relative to the position in the Periodic Table). The bond charge in $\rho_{\rm val}$ is oriented *parallel* to the bond direction. In contrast, the deformation charge density maps $\Delta\rho_{\rm tot}(\mathbf{r})$ and $\Delta\rho_{\rm val}(\mathbf{r})$ (Figs. 3 and 4) are parallel to the bond direction in C but *perpendicular* in Si and Ge. $\rho_{\rm val}(\mathbf{r})$ and $\Delta\rho_{\rm tot}(\mathbf{r})$ exhibit localized features reflecting changes in the atomic nodal structures by the crystalline environment (Figs. 4). This leads to a slow convergence of the respective Fourier series (Figs. 6 and 7). Even the state-of-art set of reflections of Cummings and Hart is insufficient for capturing such features in a Fourier synthesis. A similar situation exists for GaAs, where the measured reflections[61] are insufficient to capture many of the features of $\Delta\rho$.

(vi) *Dawson's model versus Fourier summation.* When a limited set of $\rho(\mathbf{G})$ is available, a fit to Dawson's model produces a smooth density. This reflects the fact that the model extrapolates smoothly the high-$\mathbf{G}$ components outside the set. A direct Fourier summation of a limited set of $\rho(\mathbf{G})$ can produce noisy $\rho(\mathbf{G})$. On the other hand, when a large set of $\rho(\mathbf{G})$ is available, Dawson's model produces a poor fit due to its limited flexibility to represent rapidly varying densities near the core. A direct Fourier summation of a large (converged) set of $\rho(\mathbf{G})$ produces a smooth $\rho(\mathbf{r})$.

(vii) *Static versus dynamic densities.* The conjecture of Zuo, Spence, and O'Keeffe[33] that high-momentum components will not significantly modify dynamic maps is not supported by our calculations. We find that high-momentum components affect significantly *both* static and dynamic deformation maps (Fig. 16, although dynamic maps show some broadening of the localized features near the nuclei). In view of the fact that $\Delta\rho$ do exhibit localized features, this implies that the current inability to accurately measure high Fourier components does affect the accuracy of the ensuing density maps.

(viii) *Relativistic effects in Ge.* Using relativistic free-atom structure factors in the Ge fits improves the agreement between the model and experimental forbidden structure factors (Table IX), reduces the unphysical negative valence density in the model (Fig. 10), and improves the comparison of structure factors with the *ab initio* results (Table VIII). Our predictions of the structure factors and density maps of Ge await more accurate experimental testing.

(ix) *"Forbidden" reflections.* Contributed solely by the deformations and anharmonic thermal motion, the magnitudes of these structure factors are sensitive measures for the quality of any calculation or model fit. Here, the LDA-calculated and, in particular, the model values are in very good agreement with experiment. For the highest-order measured reflections, (442) and (622), the agreement is within a few millielectrons. This lends further support and credibility to both the model and the LDA calculations.

ACKNOWLEDGMENTS

We are grateful to J. Spence and S. Froyen for stimulating discussions on the subject, to M. Spackman for useful comments, and for supplying Stewart's atomic orbital for carbon and to Gila Zipori at Bar-Ilan for expert programming assistance. The work of Z.W.L. and A.Z. was supported by the U.S. Department of Energy, Office of Energy Research, Basic Energy Science, Grant No. DE-AC02-83-CH10093.

[1] S. Cummings and M. Hart, Aust. J. Phys. **41**, 423 (1988).
[2] P. J. E. Aldred and M. Hart, Proc. R. Soc. London Ser. A **332**, 223 (1973).
[3] R. Teworte and U. Bonse, Phys. Rev. B **29**, 2102 (1984).
[4] T. Saka and N. Kato, Acta Crystallogr. Sec. A **42**, 469 (1986).
[5] M. Deutsch, Phys. Lett. A **153**, 368 (1991).
[6] M. Deutsch, Phys. Rev. B **45**, 646 (1992); see also **46**,

607(E) (1992).
[7]R. W. Alkire, W. B. Yelon, and J. R. Schneider, Phys. Rev. B **26**, 3097 (1982).
[8]P. Hohenberg and W. Kohn, Phys. Rev. **136**, B864 (1964).
[9]W. Kohn and L. J. Sham, Phys. Rev. **140**, A1133 (1965).
[10]G. P. Walter and M. L. Cohen, Phys. Rev. B **4**, 1877 (1971).
[11]J. R. Chelikowsky and M. L. Cohen, Phys. Rev. B **10**, 5095 (1974).
[12]C. M. Bertoni, V. Bortolani, C. Calandra, and F. Nizzoli, J. Phys. C **6**, 3612 (1973).
[13]A. Baldereschi, K. Maschke, A. Milchev, R. Pickenhain, and K. Unger, Phys. Status Solidi B **108**, 511 (1981).
[14]D. R. Hamann, Phys. Rev. Lett. **42**, 662 (1979).
[15]A. Zunger and M. L. Cohen, Phys. Rev. B **20**, 4082 (1979).
[16]A. Zunger, Phys. Rev. B **21**, 4785 (1980).
[17]J. Ihm and M. L. Cohen, Phys. Rev. B **21**, 1527 (1980).
[18](a) M. T. Yin and M. L. Cohen, Phys. Rev. B **26**, 5668 (1982); (b) Phys. Rev. Lett. **50**, 1172 (1983).
[19]H. Nielsen and R. M. Martin, Phys. Rev. B **32**, 3792 (1985).
[20]D. J. Stukel and R. N. Euwema, Phys. Rev. B **1**, 1635 (1970).
[21]P. M. Raccah, R. N. Euwema, D. J. Stukel, and T. C. Collins, Phys. Rev. B **1**, 756 (1970).
[22]C. S. Wang and D. M. Klein, Phys. Rev. B **24**, 3393 (1981).
[23]R. Heaton and E. Lafon, J. Phys. C **14**, 347 (1981).
[24]K. H. Weyrich, Phys. Rev. B **37**, 10 269 (1988).
[25]M. Methfessel, C. O. Rodriguez, and O. K. Andersen, Phys. Rev. B **40**, 2009 (1989).
[26]H. M. Polatoglou and M. Methfessel, Phys. Rev. B **41**, 5898 (1990).
[27]R. Dovesi, M. Causa, and G. Angonoa, Phys. Rev. B **24**, 4177 (1981).
[28]C. Pisani, R. Dovesi, and R. Orlando, Int. J. Quantum Chem. **42**, 5 (1992).
[29]L. C. Balbás, A. Rubio, J. A. Alonso, M. H. March, and G. Borstel, J. Phys. Chem. Solids **49**, 1013 (1988).
[30]M. A. Spackman, Acta Crystallogr. Sec. A **42**, 271 (1986).
[31]J. E. Bernard and A. Zunger, Phys. Rev. Lett. **62**, 2328 (1989).
[32]Z. W. Lu, S.-H. Wei, and A. Zunger, Acta Metall. Mater. **40**, 2155 (1992).
[33]J. M. Zuo, J. C. H. Spence, and M. O'Keeffe, Phys. Rev. Lett. **62**, 2329 (1989).
[34]M. Renninger, Z. Kristallogr. **97**, 107 (1937); Acta Crystallogr. Sec. A **36**, 957 (1955).
[35]R. Brill, H. G. Grimm, C. Hermann, and C. Peters, Ann. Phys. (Leipzig) **34**, 393 (1939).
[36]S. Göttlicher and E. Wölfel, Z. Elektrochem. **63**, 891 (1959).
[37]R. J. Weiss and R. Middleton (private communication).
[38]A. R. Lang and Z.-H. Mai, Proc. R. Soc. London Ser. A **368**, 313 (1979).
[39]T. Takama, K. Tsuchiya, K. Kobayashi, and S. Sato, Acta Crystallogr. Sec. A **46**, 514 (1990).
[40]T. Matsushita and K. Kohra, Phys. Status Solidi **24**, 531 (1974).
[41]S. L. Mair and Z. Barnea, J. Phys. Soc. Jpn. **38**, 866 (1975).
[42]T. Takama and S. Sato, Jpn. J. Appl. Phys. **20**, 1183 (1981).
[43]M. Deutsch, M. Hart, and S. Cummings, Phys. Rev. B **42**, 1248 (1990).
[44]M. A. Spackman, Acta Crystallogr. Sec. A **47**, 420 (1991).
[45]A. S. Brown and M. A. Spackman, Acta Crystallogr. Sec. A **46**, 381 (1990).
[46]B. Dawson, Proc. R. Soc. London Ser. A **298**, 264 (1967); **298**, 379 (1967).
[47]R. F. Stewart, J. Chem. Phys. **58**, 1668 (1973).
[48]R. F. Stewart, Acta Crystallogr. Sec. A **32**, 565 (1976).
[49]P. Coppens, T. N. Row GuRo, P. Leung, E. D. Stevens, P. J. Becker, and Y. W. Yang, Acta Crystallogr. Sec. A **35**, 63 (1979).
[50]*Electron and Magnetization Densities in Molecules and Crystals*, edited by P. Becker (Plenum, New York, 1980).
[51]E. Clementi, IBM J. Res. Dev. **9**, Suppl. 2 (1965).
[52]R. F. Stewart, in *Electron and Magnetization Densities in Molecules and Crystals* (Ref. 50), p. 427.
[53]D. T. Cromer and D. J. Liberman, J. Chem. Phys. **53**, 1891 (1970).
[54]D. T. Cromer, Acta Crystallogr. **18**, 17 (1965).
[55]D. C. Creagh, Aust. J. Phys. **41**, 487 (1988); M. Deutsch and M. Hart, Phys. Rev. B **30**, 640 (1984); **37**, 2701 (1988).
[56]D. M. Ceperley and B. J. Alder, Phys. Rev. Lett. **45**, 566 (1980).
[57]*International Tables for X-Ray Crystallography* (International Union of Crystallography, Kynoch, Birmingham, England, 1974), Vol. IV, pp. 71–98.
[58]J. Z. Tischler and B. W. Batterman, Phys. Rev. B **30**, 7060 (1984).
[59]J. B. Roberto, B. W. Batterman, and D. T. Keating, Phys. Rev. B **9**, 2590 (1974).
[60]J. E. Jaffe and A. Zunger, Phys. Rev. B **28**, 5822 (1983).
[61]J. M. Zuo, J. C. H. Spence, and M. O'Keeffe, Phys. Rev. Lett. **61**, 353 (1988).
[62]In a previous paper (Ref. 6), Deutsch used another definition for the deformation density, which included only the nonspherical components of the deformation, [the last two terms in Eq. (21)]. While the two definitions become identical for $\kappa_{nl} \equiv 1$, we will use here only the standard definition of Eqs. (20) and (21). Note that the forms (19)–(21) differ from (17b) and (18) since the former avoid explicit Fourier truncation effects.
[63]S.-H. Wei and H. Krakauer, Phys. Rev. Lett. **55**, 1200 (1985), and references therein.
[64]J. P. Perdew and A. Zunger, Phys. Rev. B **23**, 5048 (1981).
[65]H. J. Monkhorst and J. D. Pack, Phys. Rev. B **13**, 5188 (1976).
[66]J. C. Slater, *Quantum Theory of Molecules and Solids* (McGraw-Hill, New York, 1974), Vol 4.
[67]E. Wigner, Phys. Rev. **46**, 1002 (1934).
[68]L. Hedin and B. I. Lundqvist, J. Phys. C **4**, 2064 (1971).
[69]K. S. Singwi, A. Sjölander, M. P. Tosi, and R. H. Land, Phys. Rev. B **1**, 1044 (1970).
[70]O. Gunnarsson, O. Jonson, and B. I. Lundqvist, Phys. Rev. B **20**, 673 (1979).
[71]L. C. Balbás, G. Borstel, and J. A. Alonso, Phys. Lett. **114A**, 236 (1986); L. C. Balbás, J. A. Alonso, and G. Borstel, Z. Phys. D **6**, 219 (1987); L. C. Balbás, A. Rubio, J. A. Alonso, N. H. March, and G. Bostel, J. Phys. Chem. Solids **49**, 1013 (1988).
[72]J. L. Ivey, Int. J. Quantum Chem. Symp. **8**, 117 (1974).
[73]R. N. Euwema, D. L. Wilhite, and G. T. Sturratt, Phys. Rev. B **7**, 818 (1973).
[74]A. Zunger and A. J. Freeman, Phys. Rev. B **15**, 5049 (1977).
[75]W. von der Linden, P. Fulde, and K.-P. Bohnen, Phys. Rev. B **34**, 1063 (1986).
[76]R. Dovesi, C. Pisani, F. Ricca, and C. Roetti, Phys. Rev. B **22**, 5936 (1980).
[77]R. Heaton and E. Lafon, Phys. Rev. B **17**, 1958 (1978).
[78]R. Orlando, R. Dovesi, C. Roetti, and V. R. Saunders, J. Phys. Condens. Matter **2**, 7769 (1990).

[79]M. T. Yin and M. L. Cohen, Phys. Rev. B **24**, 6121 (1981).
[80]R. Jones and M. W. Lewis, Philos. Mag. B **49**, 95 (1984).
[81]P. J. H. Denteneer and W. van Haeringen, J. Phys. C **18**, 4127 (1985).
[82]P. E. van Camp, V. E. van Doren, and J. T. Devreese, Phys. Rev. B **34**, 1314 (1986).
[83]C. O. Rodriguez, R. A. Casali, Y. Peltzer, E. L. Blanca, and O. M. Cappannini, Phys. Status Solidi B **143**, 539 (1987).
[84]J. R. Chelikowsky and S. G. Louie, Phys. Rev. B **29**, 3470 (1984).
[85]G. B. Bachelet, H. S. Greenside, G. A. Baraff, and M. Schlüter, Phys. Rev. B **24**, 4745 (1981).
[86]H. Aourag, G. Merad, B. Khelifa, and A. Mahmoudi, Mater. Chem. Phys. **28**, 431 (1991).
[87]T. Kotani, T. Yamanaka, and J. Hama, Phys. Rev. B **44**, 6131 (1991).
[88]P. Trucano and B. W. Batterman, Phys. Rev. B **6**, 3659 (1972).
[89]D. Mills and B. W. Batterman, Phys. Rev. B **22**, 2887 (1979).
[90]M. L. Cohen and J. R. Chelikowsky, *Electronic Structure and Optical Properties of Semiconductors* (Springer-Verlag, Berlin, 1988).
[91]J. L. Martins and A. Zunger, J. Mater. Res. **1**, 523 (1986).
[92]In constructing this plot we have summed in Eq. (19a) over as many lattice vectors R_j as needed to converge the sum. The corresponding plot in the Deutsch paper (Ref. 5) restricted the sum to only 14 atoms so there are small differences relative to Fig. 8(b) here. These underconvergence problems have been corrected in the later paper (Ref. 6).
[93]Y. W. Yang and P. Coppens, Solid State Commun. **15**, 1555 (1974).